Title

Invasive breast cancer reprograms early myeloid differentiation in the bone marrow to generate immunosuppressive neutrophils.

Journal

Proceedings of the National Academy of Sciences of the United States of America, 112(6)

ISSN

0027-8424

Authors

Casbon, Amy-Jo
Reynaud, Damien
Park, Chanhyuk
et al.

Publication Date

2015-02-01

DOI

10.1073/pnas.1424927112

Peer reviewed

Invasive breast cancer reprograms early myeloid differentiation in the bone marrow to generate immunosuppressive neutrophils

Amy-Jo Casbon[a], Damien Reynaud[b], Chanhyuk Park[a], Emily Khuc[a], Dennis D. Gan[a], Koen Schepers[b], Emmanuelle Passegué[b], and Zena Werb[a,1]

[a]Department of Anatomy and [b]The Eli and Edythe Broad Center of Regeneration Medicine and Stem Cell Research, Department of Medicine, and Division of Hematology/Oncology, University of California, San Francisco, CA 94143

Contributed by Zena Werb, January 1, 2015 (sent for review November 24, 2014; reviewed by Douglas Fearon and Michael Karin)

Expansion of myeloid cells associated with solid tumor development is a key contributor to neoplastic progression. Despite their clinical relevance, the mechanisms controlling myeloid cell production and activity in cancer remains poorly understood. Using a multistage mouse model of breast cancer, we show that production of atypical T cell-suppressive neutrophils occurs during early tumor progression, at the onset of malignant conversion, and that these cells preferentially accumulate in peripheral tissues but not in the primary tumor. Production of these cells results from activation of a myeloid differentiation program in bone marrow (BM) by a novel mechanism in which tumor-derived granulocyte-colony stimulating factor (G-CSF) directs expansion and differentiation of hematopoietic stem cells to skew hematopoiesis toward the myeloid lineage. Chronic skewing of myeloid production occurred in parallel to a decrease in erythropoiesis in BM in mice with progressive disease. Significantly, we reveal that prolonged G-CSF stimulation is both necessary and sufficient for the distinguishing characteristics of tumor-induced immunosuppressive neutrophils. These results demonstrate that prolonged G-CSF may be responsible for both the development and activity of immunosuppressive neutrophils in cancer.

cancer | immunology | stem cell biology | hematopoiesis | myeloid-derived suppressor cells

Cancer is a systemic disease. Tumors secrete a variety of factors that not only regulate their local microenvironment, but also regulate peripheral tissues to promote metastasis (1–3). The tumor-promoting role of the immune system has long been recognized (4–7), and emerging evidence suggests that accumulation of circulating myeloid cells at peripheral sites promotes a permissive macro-environment for systemic tumor outgrowth.

In cancer patients with solid tumors, aberrant myeloid cells with T cell-suppressive activity are significantly increased in the circulation compared with healthy individuals and are highest in number in patients with extensive metastatic tumor burden (8). In murine transplantation models that mainly mimic the late stages of tumor development, T cell-suppressive myeloid cells expand in the circulation and also in the tumor, spleen, and premetastatic lungs (9). Of particular interest, these myeloid cells promote tumor progression by impairing adaptive immune responses (10, 11), modulating cytokine production by macrophages (12), and stimulating angiogenesis and remodeling of the extracellular matrix (13). In addition, expansion of these T cell-suppressive myeloid cells in premetastatic lung is associated with a local decrease in IFNγ production, the major antitumor cytokine, and an increase in several protumor cytokines, along with vascular remodeling leading to abnormal leaky vessels (14, 15).

This population of myeloid cells that acquires the ability to suppress T-cell function in cancer is heterogeneous and includes monocytes, myeloid precursors, and neutrophils, leading to the collective term myeloid-derived suppressor cells (MDSCs) (16). The T cell-suppressive phenotype is mediated by increased arginase activity and the production of reactive oxygen species (ROS) (16). These cells share common myeloid surface markers with their naïve healthy counterparts ($CD11b^+Gr1^+$ in mice or $CD11b^+CD33^+HLADR^-$ in humans), but differ in activity and gene expression. Although a link between poor prognosis in breast cancer and an increase in circulating myeloid cells in humans is well documented (17), how tumors regulate myeloid cell development remains largely unknown.

Hematopoietic cells are all produced from a rare population of self-renewing hematopoietic stem cells (HSCs), which reside in the bone marrow (BM) cavity (18). In mice, the $lineage^{neg}$ $Sca\text{-}1^+c\text{-}Kit^+$ (LSK) cell compartment contains the most immature hematopoietic stem and progenitor cells (HSPCs) and include HSCs (defined as LSK $Flk2^{neg}CD150^+CD48^{neg}$) along with non–self-renewing multipotent progenitors (MPPs), which can be further divided into LSK $Flk2^+$ (MPP^{F+}) and a less characterized LSK $Flk2^{neg}CD48^+$ (MPP^{F-}) subset (19). MPPs give rise to lineage-committed common lymphocyte progenitors (CLPs) and common myeloid progenitors (CMPs, defined as $lineage^{neg}Sca\text{-}1^+c\text{-}Kit^{neg}Fc\gamma R^{neg}CD34^+$), which support the production of all circulating mature lymphoid and myeloid cells, respectively. CLPs give rise to distinct subsets of B cells, T cells, natural killer cells, and dendritic cells (DCs), whereas CMPs differentiate into granulocyte/macrophage progenitors (GMPs, defined as $lineage^{neg}Sca\text{-}1^+c\text{-}Kit^{neg}Fc\gamma R^+CD34^+$) to support the produc-

Significance

We show that tumor reprogramming of hematopoiesis in bone marrow occurs at the onset of malignant conversion and results in systemic expansion of circulating activated neutrophils that preferentially accumulate in lungs. Our data are, to our knowledge, the first to show that activation and not inhibition of myeloid differentiation is responsible for expansion and activity of T cell-suppressive myeloid cells; a tumor-derived factor targets the immature hematopoietic compartment to drive myeloid expansion; granulocyte-colony stimulating factor (G-CSF) is the only hematopoietic growth factor to increase in serum during early tumor development; prolonged G-CSF induces production of $Rb1^{low}$ neutrophils and not short-term mobilization; and G-CSF acts in a cell intrinsic manner to expand multipotent progenitors to increase production of tumor-derived $Ly6G^+$ neutrophils.

Author contributions: A.-J.C., E.P., and Z.W. designed research; A.-J.C., D.R., C.P., E.K., D.D.G., and K.S. performed research; A.-J.C., D.R., and K.S. analyzed data; and A.-J.C. and Z.W. wrote the paper.

Reviewers: D.F., Cold Spring Habor Laboratory; and M.K., University of California, San Diego School of Medicine.

The authors declare no conflict of interest.

[1]To whom correspondence should be addressed. Email: zena.werb@ucsf.edu.

This article contains supporting information online at www.pnas.org/lookup/suppl/doi:10.1073/pnas.1424927112/-/DCSupplemental.

tion of monocytic (macrophage) and granulocytic (neutrophils, eosinophils, and basophils) cells, as well as myeloid-derived DCs. CMPs also differentiate into megakaryocyte/erythrocyte progenitors (MEPs, defined as lineage^{neg}Sca-1^{+}c-Kit^{neg}FcγR^{neg} CD34^{neg}) to give rise to red blood cells (RBCs) and megakaryocytes (platelets). Within this well-established hematopoietic tree, the origin of tumor-associated T cell-suppressive CD11b^{+}Gr1^{+} myeloid cells is still a matter of debate.

The current model suggests that these cells arise from myeloid progenitors (MPs) that are past the GMP stage in a two-step process that includes a block in differentiation, resulting in an expansion of CD11b^{+}Gr1^{+} myeloid precursors and an induction of T cell-suppressive activity (9). Tumor-derived myeloid differentiation cytokines including granulocyte (G)-colony stimulating factor (G-CSF), macrophage (M)-colony stimulating factor (CSF), and GM-CSF are thought to induce accumulation of immature myeloid progenitors, in combination with tumor-associated proinflammatory factors (e.g., IL-1β, IL-6, S100A8, S100A9). In addition, T cell-derived cytokines (IFNγ, IL-4, IL-10, and IL-13) likely commit T cell-suppressive activity to these cells (9). Epigenetic silencing of the gene that encodes the protein for Retinoblastoma-1 (Rb1) is also associated with the aberrant myeloid cell expansion that occurs in solid tumor cancers, and knockdown of Rb1 in the absence of tumor development is sufficient to induce the overproduction of similar myeloid cells, but without T cell-suppressive activity (20). Although these results provide a mechanism for the expansion of tumor-associated CD11b^{+}Gr1^{+} myeloid cells, it remains unknown which tumor-secreted factors inhibit Rb1 expression, at which stage during myeloid commitment loss of Rb1 occurs, and how T cell-suppressive activity is acquired. Moreover, it remains unclear whether this effect is limited to MPs or also involves more immature HSPCs.

Our goal was to determine the driving factor(s) and identify the cell populations responsible for expansion of T cell-suppressive myeloid cells in cancer. We conducted a comprehensive in vivo evaluation of the HSPC and MP regulation in an autochthonous multistage mouse model of breast cancer. We identified a previously unidentified pathway of myeloid differentiation in cancer in which tumor-derived G-CSF directs myeloid differentiation at the primitive HSC to generate activated, Rb1^{low}, T cell-suppressive neutrophils.

Results

A Coordinated Expansion of CD11b^{+}Gr1^{+} Myeloid Cells in Peripheral Tissues Parallels Tumor Development. In cancer patients, expansion of T cell-suppressive myeloid cells correlates with tumor stage (8). We used the PyMT transgenic mouse model (21), which expresses the polyomavirus middle T antigen driven by the mouse mammary tumor virus (MMTV) promoter, to map expansion of CD11b^{+}Gr1^{+} myeloid cells during the multiple stages of breast cancer progression. PyMT mice develop a progressive disease that mimics human pathology (22), in which all mammary glands (MGs) display signs of breast cancer with an initial presentation of hyperplasia (6 wk), which then transitions to adenoma or mammary intraepithelial neoplasia (8 wk), early carcinoma (10 wk), and then late-stage carcinoma (11–15 wk) (Fig. S1 *A* and *B*). Similar to human disease, mammary tumor growth is associated with the dissemination of cancer cells in the periphery and notably the lungs. We detected disseminated tumor cells (DTCs) by real-time quantitative PCR (qPCR) in the lungs of three of five PyMT mice as early as 6 wk of age (Fig. S1*C*). At 14 wk, we detected metastases, and PyMT expression increased dramatically (Fig. S1*D*).

The expansion of CD11b^{+}Gr1^{+} cells occurs within tumors, but also in blood, spleen, and premetastatic lung in murine transplantation models that mimic the late stages of tumor development (9). However, the kinetics of expansion and the location of these myeloid cells during cancer initiation and the early stages of tumor progression remain unknown. To address this question, we analyzed the frequency and cell number of CD11b^{+}Gr1^{+} cells in different tissues isolated from PyMT mice at the onset and during the course of disease (from 6 to 15 wk). To discriminate between circulating and tissue resident myeloid cells, we harvested tissues after vascular flushing. Interestingly, the proportion of CD11b^{+}Gr1^{+} cells within the developing primary tumors remained constant and below 0.4% of total cells for all tumor stages (Fig. 1*A* and Fig. S1*C*). In contrast, we detected a significant systemic increase in proportion and number of these cells in the lung, blood, and spleen at 10 wk, with a continued increase with age (Fig. 1*A* and Fig. S2 *A*–*C*). Thus, we evaluated the proportion of CD11b^{+}Gr1^{+} cells within the CD45^{+} immune compartment in the primary tumor and lung. CD11b^{+}Gr1^{+} cells represented 8% of CD45^{+} cells in late-stage tumors, but they made up 39% in lungs (Fig. S2*D*). These data show a coordinated expansion of CD11b^{+}Gr1^{+} cells in peripheral tissues during early tumor development and provide a model system to decipher the mechanism for expansion of these cells in cancer.

Activated CD11b^{+}Ly6G^{+} Neutrophils Are the Predominant Myeloid Cell Type That Expand in Peripheral Tissues During Tumor Progression. The Gr1 antibody recognizes two antigens: Ly6G, a specific marker for neutrophils (23), and Ly6C, which is expressed on myeloid and nonmyeloid cells (24). Two distinct subsets of Gr1^{+} myeloid cells, polymorphonuclear (PMN) CD11b^{+}Ly6G^{+}Ly6C^{int} (referred to as Ly6G^{+}) and monocytic (Mo) CD11b^{+}Ly6G^{-}Ly6C^{hi} (referred to as Ly6C^{hi}) (also called PMN-MDSCs and Mo-MDSCs, respectively) (25) expand in cancer, both with T cell-suppressive activity. We found that Ly6G^{+} cells were the predominant Gr1^{+} cell subset that increased substantially in all tissues from PyMT mice (Fig. 1*B* and Fig. S3 *A* and *B*). Ly6G^{+} cells from PyMT mice showed typical neutrophil morphology (Fig. 1*B*).

A distinguishing characteristic of Ly6G^{+} cells in tumor-bearing mice is their ability to suppress T-cell function (26). To determine whether Ly6G^{+} cells acquired this ability in these mice, we isolated them by flow cytometry from spleens and cocultured them with carboxyfluorescein diacetate succinimidyl ester (CFSE)-labeled splenocytes, in the presence of anti-CD3 and anti-CD28 activating antibodies to stimulate T-cell proliferation. Ly6G^{+} cells from PyMT mice reduced both CD4 and CD8 T-cell proliferation by ∼50%, whereas Ly6G^{+} cells from WT mice did not (Fig. 1*C* and Fig. S3*C*). Because T-cell suppression by Ly6G^{+} cells is attributed to enhanced production of ROS (27), we next used a flow cytometry-based assay to assess superoxide production. In the absence of exogenous stimulation, Ly6G^{+} cells in blood and lung of tumor-bearing mice showed increased dihydrorhodamine (DHR) fluorescence, a probe that detects intracellular superoxide, indicating that neutrophils in tumor-bearing mice actively produce more ROS compared with WT mice (Fig. 1*D* and Fig. S3*D*). We also observed that total splenocytes and FACS-sorted Ly6G^{+} cells from PyMT mice had lost Rb1 expression, confirming that the loss of Rb1 is a distinct phenotype of Ly6G^{+} cells from tumor-bearing mice (20) (Fig. 1*E*). Taken together, these data demonstrate that breast cancer development in PyMT mice leads to the generation of T cell-suppressive, activated Ly6G^{+} neutrophils in peripheral tissues.

Breast Cancer Development Results in Profound Remodeling of BM Hematopoiesis. To determine the origin of Ly6G^{+} cells associated with tumor development, we assessed proliferation of Ly6G^{+} cells by BrdU incorporation (Fig. 2, *A*–*C* and Fig. S4 *A*–*C*). We did not detect any BrdU^{+} Ly6G^{+} cells in blood, lung, or MG (tumor) from WT or PyMT mice (14–15 wk) after a 2-h BrdU chase, suggesting that these organs do not significantly contribute to their production (Fig. S4 *A* and *B*). In contrast, ∼5% of Ly6G^{+} cells in BM were BrdU^{+} in both WT and tumor-bearing

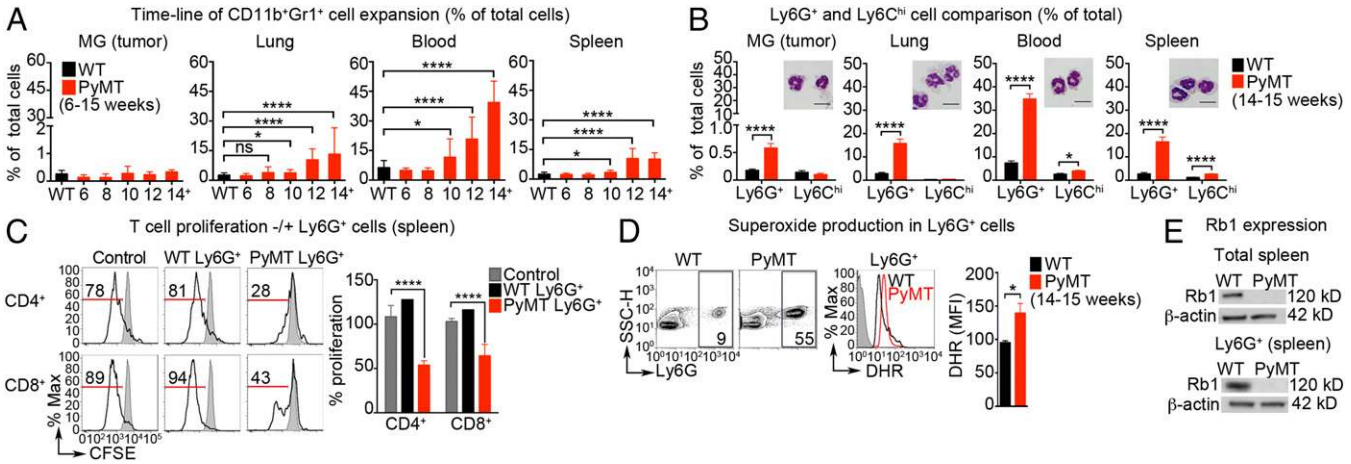

Fig. 1. Activated, T cell-suppressive Ly6G$^+$ neutrophils are the predominant myeloid cells to expand in peripheral tissues during early tumor progression. (*A*) Quantification of the frequency (% of total) of CD11b$^+$Gr1$^+$ cells in WT and PyMT mice (6–15 wk). $P > 0.05$ was not significant (ns). (*B*) Quantification of the frequency (% of total) of Ly6G$^+$ or Ly6C^{hi} cells. Wright-Giemsa (WG) staining of FACS-sorted Ly6G$^+$ cells from PyMT mice (*Insets*). (Scale bar, 10 μm.) (*C*) Representative histograms show CFSE fluorescence in unstimulated (gray-shaded) and CD3/CD28-stimulated (black line) CD4$^+$ and CD8$^+$ T cells. Values shown are the % of CD4$^+$ or CD8$^+$ T cells that proliferated (red bar) in the absence (served as the control) or presence of Ly6G$^+$ cells from WT or PyMT spleen. Quantification of CD4$^+$ and CD8$^+$ T-cell proliferation in the absence (control) or presence of WT or PyMT Ly6G$^+$ cells from the spleen. Values shown are the frequency of T cells that proliferated normalized to the control. (*D*) Superoxide production in Ly6G$^+$ cells in blood was assessed using DHR and flow cytometry. FACS plots illustrate the frequency (% of total) of Ly6G$^+$ cells and the histogram shows DHR fluorescence in Ly6G$^+$ cells. Bar graphs summarize the median fluorescent intensity (MFI) of DHR in Ly6G$^+$ cells. (*E*) Rb1 protein expression in total splenocytes (*Left*) and FACS-sorted Ly6G$^+$ cells (*Right*) was assessed by Western blot. Data are representative of (*A* and *B*) six experiments at each time point (mean ± SEM, $n = 8$–15) or two experiments (WG staining, $n = 2$), (*C*) two experiments (mean ± SEM of four samples), (*D*) three experiments (mean ± SEM, $n = 5$–6), and (*E*) four experiments (blots for total splenocytes; $n = 4$–6 biological samples) and two experiments (blots for FACS-sorted Ly6G$^+$ cells; $n = 2$ biological samples). *$P < 0.05$, **$P < 0.01$, ***$P < 0.005$, ****$P < 0.001$.

mice after a 2-h chase (Fig. 2*B*), suggesting that Ly6G$^+$ cells are generated in BM. After a 24-h chase, 40 ± 5% Ly6G$^+$ cells were BrdU$^+$ in BM of PyMT mice, which was significantly more than in BM of WT mice in which 25 ± 2% were BrdU$^+$ (Fig. 2*C*). Of note, only Ly6G^{low} cells incorporated BrdU after a 2-h BrdU chase, whereas Ly6G$^{med/hi}$ cells showed BrdU incorporation after a 24-h chase. Thus, these data indicate that Ly6G^{low} cells are immature granulocytes that give rise to mature Ly6G^{hi} neutrophils with little proliferation potential (28). Consistent with this idea, we found that CD11b$^+$Gr1$^+$ cells dramatically expand in BM at 10 wk due to a predominant increase in Ly6G$^+$ cells (Fig. 2*D* and Fig. S4 *D* and *E*). We also detected BrdU$^+$ Ly6G$^+$ cells in spleen following a 2-h chase (Fig. 2*B*), but the frequency was approximately one third in spleen of PyMT mice compared with WT after a 24-h chase (Fig. 2, *B* and *C*), and the cell number was less than 10% compared with BM (Fig. S4*C*). These data demonstrate that the BM is the main production site of Ly6G$^+$ cells during breast tumor development.

The pale appearance of the BM from late-stage, tumor-bearing PyMT mice (Fig. 2*E* and Fig. S4*F*) and their severe anemia (Fig. S4*G*) suggested that tumor growth in the breast induces a profound alteration of BM hematopoiesis. Therefore, we examined changes in MPs and more immature HSPCs in BM of late-stage PyMT mice (Fig. 2*F*). We detected higher frequencies of GMPs within the MP population associated with an overall increase of their absolute numbers in PyMT mice compared with WT controls (Fig. 2, *G* and *H*). Although there was no significant change in CMPs, the LSK population expanded approximately twofold, with a significant increase in cell number of HSCs, MPP^{F-}, and MPP^{F+} populations (Fig. 2, *G* and *I*). We next performed longitudinal studies to determine the kinetics of HSPC expansion in early tumor-bearing PyMT mice. Strikingly, we found that HSCs expanded as early as 8 wk, whereas both MPP^{F+} and MPP^{F-} expanded at 10 wk in PyMT mice (Fig. 2*I* and Fig. S4*H*), concomitant with the increased CD11b$^+$Gr1$^+$ cells in peripheral tissues (Figs. 2*D* and 1). Thus, expansion of HSCs occurred during early tumor development, followed by expansion of MPPs and CD11b$^+$Gr1$^+$ myeloid cells as early as 10 wk, suggesting activation of HSCs leads to increased production of MPPs, which then gives rise to an expanded myeloid compartment.

Expansion of T cell-suppressive myeloid cells in cancer is associated with enlargement of the spleen (29), which may act as a reservoir for extramedullary hematopoiesis (30). We also observed an enlarged spleen in late-stage PyMT mice (Fig. S5*A*); thus, we also assessed MP and HSPC populations in the spleen. Unlike BM, the majority (80–90%) of spleen-residing MPs were MEPs (Fig. S5*B*), which increased in numbers approximately sixfold in PyMT mice (Fig. S5 *C* and *D*). No difference in the frequencies of MPP^{F+}, MPP^{F-}, or HSCs was observed (Fig. S5*B*), although the total number of these cells was higher than in WT mice (Fig. S5*E*) due to the increased size of the spleen in late-stage PyMT mice (Fig. S5 *A* and *C*). Increased production of Ly6G$^+$ cells combined with an increase in the frequency of HSCs, MPPs, and GMPs in BM, but not spleen, suggests activation of a specific myeloid differentiation pathway in BM of tumor-bearing mice.

G-CSF Is Necessary and Sufficient for the Activated and Rb1^{low} Phenotype of Immunosuppressive Neutrophils. We next hypothesized that the factor(s) driving expansion of Ly6G$^+$ cells would be present in the serum of PyMT mice. When we assessed the serum concentration of several cytokines and chemokines, only a few factors were increased systemically during early carcinoma formation (10 wk), whereas multiple factors were deregulated during late-stage tumor progression (>12 wk) (Fig. 3*A* and Table S1). Notably, G-CSF and the neutrophil-attracting chemokine CXCL1 (KC), and to a lesser extent CCL2 (MCP-1), increased early during disease development (Fig. 3*A*). In contrast, the related myeloid growth factors GM-CSF and M-CSF and chemokines CCL3 and CCL4 did not increase during the early phase of tumor progression (Fig. 3*A*). We also detected abundant secretion of G-CSF and CXCL1, but not CCL2, in the supernatants of cultured primary PyMT tumor cells (Fig. 3*B*) and the VO-PyMT

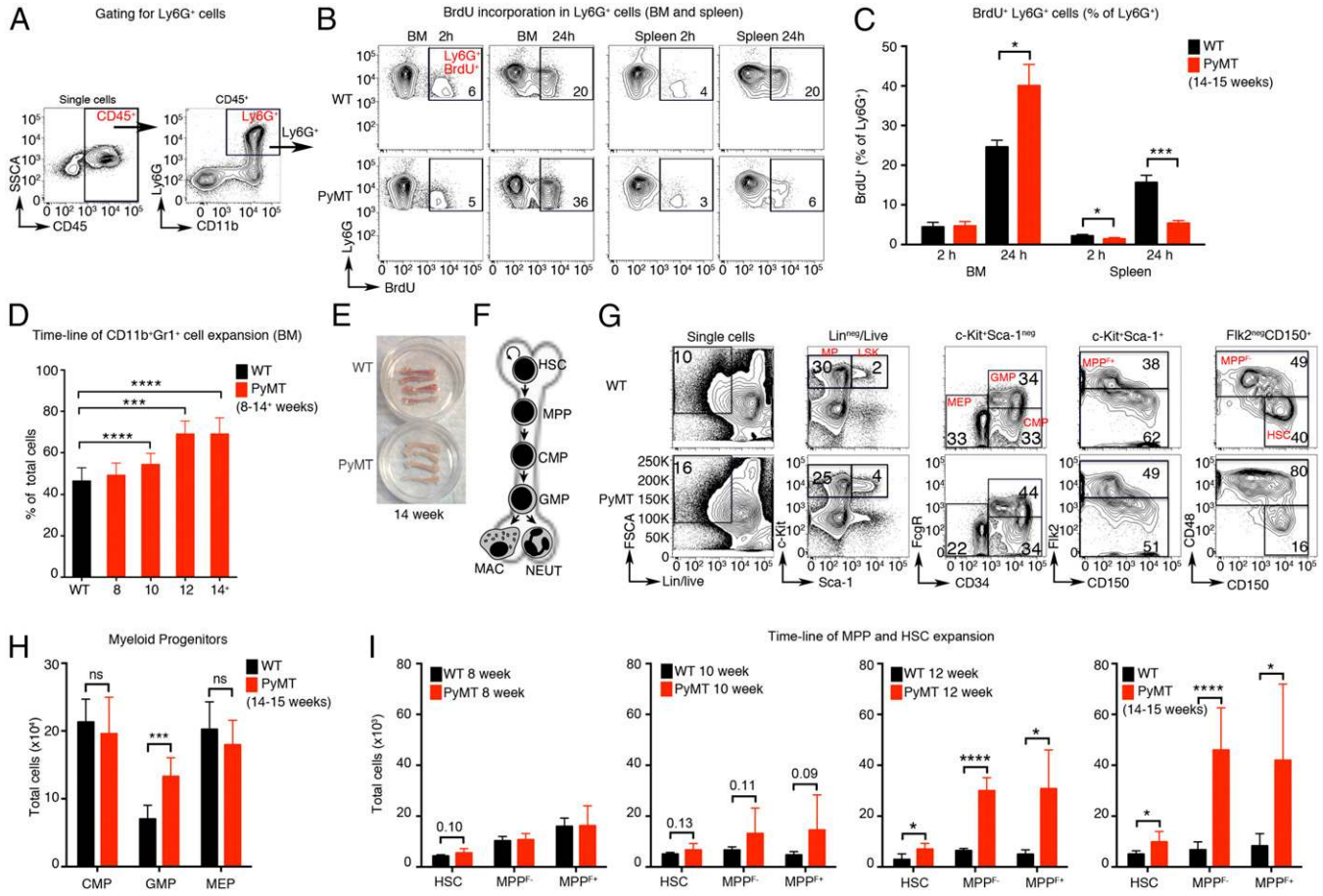

Fig. 2. Breast cancer development results in profound remodeling of BM hematopoiesis. (*A*) Gating strategy to evaluate BrdU incorporation in Ly6G$^+$ cells by flow cytometry. (*B*) Representative FACS plots of BrdU incorporation (2 and 24 h after i.p. injection) in Ly6G$^+$ cells in BM and spleen of WT and PyMT FVB/n mice (14–15 wk). (*C*) Summary of the % of Ly6G$^+$ cells that are BrdU$^+$ in BM and spleen at 2 and 24 h. (*D*) Frequency (% of total) of CD11b$^+$Gr1$^+$ cells in BM of WT and PyMT FVB/n mice during tumor progression (8–15 wk). (*E*) Representative image of femurs and tibias from WT and PyMT FVB/n mice. (*F*) Schematic of myeloid differentiation. (*G–I*) The frequency and total cell numbers of MPs and HSPCs were evaluated in BM of WT and PyMT FVB/n mice (14–15 wk) by flow cytometry. (*G*) FACS plots illustrate the gating for MP, MPP, and HSC populations. Values shown are the frequency of cells within each parent gate. (*H*) Total cell numbers of MP subpopulations (CMP, GMP, and MEP). (*I*) Total cell numbers of HSCs and MPPs (MPP^{F-} and MPP^{F+}) in BM of WT and PyMT FVB/n mice (8–12 wk). Data are representative of (*A–C*) two experiments (mean ± SD, n = 3–4), (*D*) four experiments at each time point (mean ± SD, n = 10–12), (*E*) six experiments (n = 8–15), (*H*) three experiments (mean ± SD, n = 5–7), (*I*) three experiments (8 and 10 wk; mean ± SD, n = 5), two experiments (12 wk; mean ± SD, n = 6–7), and five experiments (14–15 weeks; mean ± SD, n = 5–9). *P < 0.05, **P < 0.01, ***P < 0.005, ****P < 0.001.

cell line (Fig. 3*C*), pointing to the tumor cells as the source of these systemic factors.

Given that G-CSF was recently shown to promote tumor progression by contributing to the T cell-suppressive activity of neutrophils (31), we asked whether G-CSF contributed to the activated phenotype of Ly6G$^+$ cells in PyMT mice. Although Ly6G$^+$ cells from control antibody-treated PyMT mice had increased ROS production compared with WT mice, Ly6G$^+$ cells from PyMT mice treated with a neutralizing antibody to G-CSF did not (Fig. 4*A*). Anti–G-CSF treatment also reduced the frequency of circulating Ly6G$^+$ cells (Fig. 4*A*) and the concentration of G-CSF in the serum of PyMT mice (Fig. 4*B*). Next, we assessed whether G-CSF was sufficient to induce ROS production. We stimulated WT mice for 5 consecutive days with G-CSF (2 μg/mouse), a dose that recapitulates the persistent high levels detected in late-stage PyMT mice (Fig. 4*C*). Indeed, G-CSF stimulation alone increased ROS production in Ly6G$^+$ cells (Fig. 4*D*). Thus, tumor-derived G-CSF was both necessary and sufficient for enhanced ROS production in Ly6G$^+$ cells in PyMT mice.

We then investigated whether tumor-derived G-CSF also regulated the loss of Rb1 in activated Ly6G$^+$ cells. Anti–G-CSF treatment of late-stage PyMT mice restored Rb1 protein expression in splenocytes (Fig. 4*E*). In addition, Rb1 expression decreased in total splenocytes and isolated Ly6G$^+$ cells from WT mice stimulated with G-CSF for 3 d, but not 1 d, and decreased in a time-dependent manner thereafter to levels similar to late-stage PyMT mice (Fig. 4*F*). To assess the kinetics in the loss of Rb1 expression in Ly6G$^+$ cells from multiple tissues, we used a more sensitive intracellular flow cytometry assay (Fig. 4*G*). Rb1 expression was strongly expressed in circulating Ly6G$^+$ cells in spleen and blood of WT mice. Surprisingly, Ly6G$^+$ cells from BM of WT and PyMT mice did not express Rb1. These results suggest that Rb1 expression is normally acquired in circulating Ly6G$^+$ cells after they leave the BM in WT mice, and its acquisition is inhibited by tumor-derived G-CSF. Thus, tumor-derived G-CSF is the key factor responsible for the two distinguishing characteristics of tumor-derived immunosuppressive neutrophils: enhanced ROS production and loss of Rb1 expression.

Tumor-Derived G-CSF Targets Hematopoietic Stem and Early Progenitors to Drive Myeloid Cell Production in BM. To test the involvement of G-CSF in activating myeloid cell production in tumor-bearing mice, we treated WT and PyMT mice with the

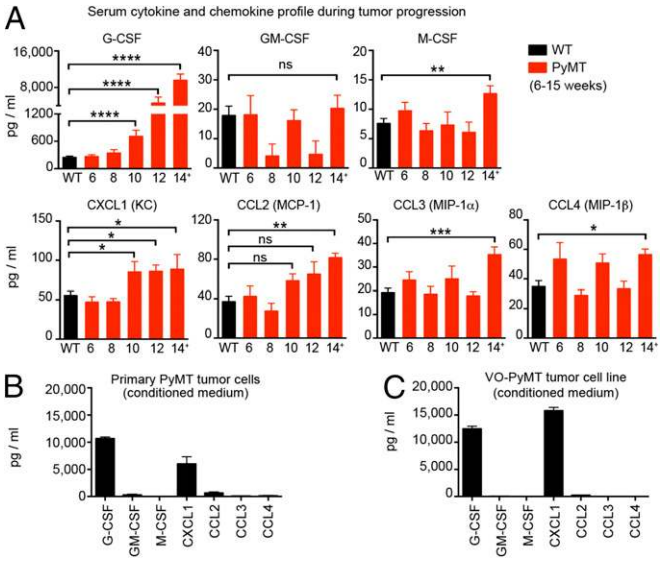

Fig. 3. Tumor-derived G-CSF, not GM-CSF or M-CSF, increases systemically during early tumor progression. Concentrations of G-CSF, GM-CSF, M-CSF, CXCL1, CCL2, CCL3, and CCL4 in (*A*) serum from WT and PyMT FVB/n mice (6–15 wk) and conditioned medium collected from (*B*) primary PyMT C57BL/6 tumor cells and (*C*) FVB/n VO-PyMT cell line were determined using multiplex laser bead technology (Eve Technologies). Data are representative of (*A*) two or three experiments (mean ± SEM, $n = 4$–7) and (*B* and *C*) two experiments, each sample in duplicate (mean ± SD of four biological samples). $^{*}P < 0.05$, $^{**}P < 0.01$, $^{***}P < 0.005$, $^{****}P < 0.001$.

anti-G-CSF antibody. As expected, blocking G-CSF reduced systemic levels of $CD11b^{+}Gr1^{+}$ cells in all tissues in WT and PyMT mice (Fig. S6 *A*–*C*). Importantly, blocking G-CSF not only reduced $Ly6G^{+}$ neutrophils, but also returned $Ly6C^{hi}$, MPP^{F+}, MPP^{F-}, and HSC numbers to WT levels in BM of tumor-bearing mice while having no significant effect on MPP and HSC numbers in WT mice (Fig. 5*A* and Fig. S6*D*). In addition, the altered phenotypes of the BM and spleen that are characteristic of myeloid dysregulation were restored to WT conditions after anti–G-CSF treatment (Fig. 5*B*).

Next, we assessed whether G-CSF stimulation alone was sufficient to expand mature myeloid cells, as well as early progenitors in WT mice. After 1 d of G-CSF stimulation, $Gr1^{+}$ cells and specifically $Ly6G^{+}$ cells increased in blood, but not in BM or spleen (Fig. 5, *C* and *D* and Fig. S7*A*), supporting mobilization of $Ly6G^{+}$ cells from BM by G-CSF. Of note, an increase in $Ly6G^{low}$ cells was observed in BM after 1 d and was more evident after 3 d of G-CSF stimulation (Fig. 5*D*), consistent with production of immature neutrophils (32, 33). We also observed a similar increase in $Ly6G^{low}$ cells in blood and spleen, but not until 3 d of G-CSF stimulation (Fig. 5*D*), which suggests that this increase was due to increased production of $Ly6G^{+}$ cells from the BM. In addition, an increase in GMPs and the loss of red pigment in the BM was also observed after 3 d of G-CSF stimulation (Fig. 5, *E* and *F* and Fig. S7*B*). Importantly, 12 h and 1 d of G-CSF stimulation was sufficient to increase MPPs, which continued to increase after 3 and 5 d of stimulation (Fig. 5*G* and Fig. S7*B*). During most of the treatment, the number of HSCs did not significantly change despite a minor and transient increase after 12 h of G-CSF stimulation (Fig. 5*G*). In contrast to BM, 12-h G-CSF stimulation did not increase HSCs or MPPs in the spleen (Fig. 5*H*). The kinetics of expansion of these BM populations suggests a rapid activation of a myeloid differentiation program in the early hematopoietic compartment by prolonged G-CSF stimulation (>1 d). These data show that G-CSF is necessary and sufficient for tumor reprogramming of hematopoietic differentiation in the BM in cancer.

G-CSF Acts in a Cell Intrinsic Manner to Drive Altered Myeloid Differentiation in Cancer. To demonstrate the role of G-CSF in activating myeloid differentiation in the early hematopoietic compartments in tumor-bearing mice directly, we developed an orthotopic transplantation model (Fig. 6*A*). First we established mixed BM chimeras by transplanting lethally irradiated WT (CD45.1) mice with a 1:1 ratio of WT (CD45.1) and G-CSF-$R^{-/-}$ (CD45.2) BM cells. Then, following BM reconstitution, we orthotopically transplanted primary C57BL/6 late-stage PyMT tumor cells or vehicle (sham-treated) into chimeric mice. Similar to PyMT transgenic mice, we found expansion of $Ly6G^{+}$ cells in lung, blood, spleen, and BM (Fig. 6*B*), consistent with elevated G-CSF production by primary C57BL/6 late-stage PyMT tumor cells (Fig. 3*B*). We observed a highly significant expansion of GMPs, MPPs, and HSCs, but no expansion of CMPs in orthotopically transplanted mice (Fig. 6*C*), similar to changes in FVB/n PyMT transgenic mice (Fig. 2, *H* and *I*). Chimerism analyses showed a defect in the ability of G-CSF-$R^{-/-}$ cells to contribute to the expanded GMP compartment in tumor-bearing mice (Fig. 6*D*), which was expected because G-CSF is known to regulate GMPs directly (34). However, G-CSF-$R^{-/-}$ cells did not contribute to the expanded MPP compartment, and there was an overrepresentation of these cells in the expanded HSC compartment in tumor-bearing mice (Fig. 6*E*). These results confirm the engraftment of G-CSF-$R^{-/-}$ HSCs and demonstrate their inability to contribute to the activated myeloid differentiation in the BM of tumor-bearing mice. The specific expansion of G-CSF-$R^{-/-}$ HSCs may result from their inability to differentiate into MPPs or their inadequate mobilization compared with WT HSCs in the G-CSF–rich milieu of tumor-bearing mice, although we cannot rule out that other tumor-derived factors may increase HSC numbers in these animals. Taken together, these data directly demonstrate that G-CSF produced by tumor cells activates a myeloid differentiation program in the early hematopoietic compartment, before the more committed CMPs, to skew hematopoiesis toward the myeloid lineage in the BM, resulting in increased production of a specific neutrophil subset, which on circulation in the periphery, acquires an activated, T cell-suppressive, and $Rb1^{low}$ phenotype (Fig. 6*F*).

Discussion

In our study, we show that tumor-induced T cell-suppressive $Ly6G^{+}$ myeloid cells are generated from an expanded stem and early progenitor compartment, which includes HSCs, $MPPs^{F+}$, and $MPPs^{F-}$, along with GMPs in BM of tumor-bearing mice. Using longitudinal studies in a multistage transgenic mouse model, we documented an activated myeloid differentiation pathway in which HSCs and MPPs expand in parallel with $Ly6G^{+}$ and $Ly6C^{hi}$ cells at the onset of malignant conversion (8–10 wk) and continue to expand during tumor development. We confirmed activation of a similar myeloid differentiation pathway in an orthotopic transplant model of breast cancer. Although expansion of tumor-induced T cell-suppressive $Ly6C^{hi}$ and $Ly6G^{+}$ myeloid cells has been hypothesized to result from expansion of monocyte and granulocyte precursors due to a block in myeloid differentiation downstream of CMPs (27), our data show that expansion of T cell-suppressive neutrophils in cancer is not the result of a significant block in differentiation but rather targeted reprogramming of myeloid differentiation from an early hematopoietic compartment.

By defining the time-dependent expansion of T cell-suppressive myeloid cells that occurred during tumor development in PyMT mice, we showed that the myeloid differentiation factor G-CSF, and not M-CSF or GM-CSF, increases in the serum during early tumor development. Using a loss-of-function ap-

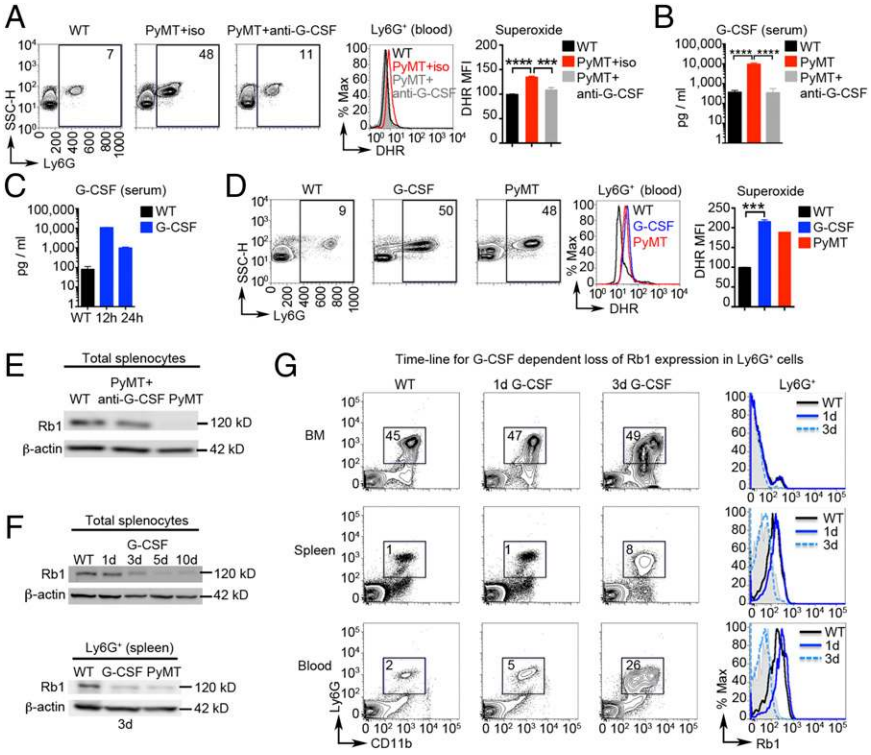

Fig. 4. G-CSF is sufficient for the enhanced ROS activity and Rb1^{low} phenotype of tumor-induced Ly6G$^+$ neutrophils. (*A*) Superoxide production was assessed by DHR fluorescence in Ly6G$^+$ cells in blood from WT and isotype or anti–G-CSF–treated PyMT FVB/n mice (14–15 wk). Representative FACS plots illustrate the frequency (% of total) of Ly6G$^+$ cells (*Left*), histogram illustrates DHR fluorescence in Ly6G$^+$ cells (*Center*), and bar graphs summarize the MFI of DHR in Ly6G$^+$ cells (*Right*). Multiplex laser capture technology (Eve Technologies) was used to measure the concentration of G-CSF in the serum from (*B*) WT, PyMT, and anti–G-CSF–treated PyMT FVB/n mice (14–15 wk) and (*C*) PBS control treated or G-CSF–stimulated (12 or 24 h) WT mice. (*D*) Superoxide production was assessed by DHR fluorescence in Ly6G$^+$ cells in blood from WT, G-CSF–stimulated, and PyMT FVB/n mice (14–15 wk). Representative FACS plots illustrate the frequency (% of total) of Ly6G$^+$ cells (*Left*), histogram illustrates DHR fluorescence in Ly6G$^+$ cells (*Center*), and bar graphs summarize the MFI of DHR in Ly6G$^+$ cells (*Right*). (*E* and *F*) Rb1 expression was assessed by Western blot in (*E*) total splenocytes and (*F*) total splenocytes (*Upper*) or FACS-sorted Ly6G$^+$ cells from the spleen (*Lower*). WT or PyMT FVB/n mice (14–15 wk). (*G*) FACS plots illustrate the frequency (% of total) of Ly6G$^+$ cells and histograms illustrate intracellular Rb1 expression in Ly6G$^+$ cells, assessed by flow cytometry. Data are representative of (*A*) two experiments (mean ± SEM, n = 3–4), (*B*) two experiments (mean ± SEM, n = 6), (*C*) one experiment (n = 2–4), (*D*) two experiments (mean ± SEM, n = 3–4), (*E* and *F*) two experiments (n = 2–3 biological samples), and (*G*) two experiments (n = 4). $^*P < 0.05$, $^{**}P < 0.01$, $^{***}P < 0.005$, $^{****}P < 0.001$.

proach with a blocking antibody to G-CSF, we demonstrated that tumor-derived G-CSF is necessary for the expansion of HSC, MPP^{F+}, MPP^{F-}, GMP, and more mature Ly6G$^+$ and Ly6C^{hi} cells in the BM of tumor-bearing mice. Furthermore, G-CSF is sufficient to rapidly expand these populations. A thorough analysis of the kinetics in myeloid expansion following G-CSF stimulation showed HSCs, along with MPP^{F+} and MPP^{F-} populations increased as early as 12 h, whereas GMPs did not increase until 3 d after stimulation, revealing that the early hematopoietic compartment is the primary target of tumor-derived G-CSF and a novel mechanism by which tumors expand Ly6G$^+$ and Ly6C^{hi} myeloid cells in cancer.

G-CSF is a complex pleiotropic cytokine that regulates neutrophil production and function, along with HSC mobilization and proliferation, although less is known about the latter (35, 36). G-CSF is believed primarily to regulate the more committed CMP and GMP populations to increase neutrophil production (35), but we demonstrated that G-CSF expands the less committed HSC and MPP populations. We found G-CSF to act in a cell intrinsic manner to expand MPPs and GMPs, but HSC expansion appeared to occur indirectly in tumor-bearing mice. Although prolonged G-CSF stimulation alone may induce quiescence and inhibit HSC function (36), we found increasing levels of G-CSF induced a linear expansion of MPP, GMP, and mature neutrophil populations while maintaining an increase in HSC numbers over the course of tumor development (10–15 wk). Thus, it is likely that the tumor microenvironment provides an additional factor(s) to maintain HSC numbers.

We showed that G-CSF drives expansion and differentiation of the early hematopoietic compartment to generate Rb1^{low}, Ly6G^{low} neutrophils in PyMT mice. Importantly, the loss of Rb1 expression was not observed after mobilization of mature neutrophils following short-term G-CSF stimulation, but was associated with new production of Ly6G^{low} immature neutrophils. Because G-CSF is known to shorten the passage time of neutrophils in the BM (37), the Rb1^{low} phenotype may reflect new production of less mature Ly6G$^+$ neutrophils by G-CSF. In two different mouse models of breast cancer (4T1 and PyMT), Kowanetz et al. also showed tumor-derived G-CSF can induce systemic accumulation of Ly6G$^+$ cells (15); however, the mechanism by which G-CSF induced expansion was not investigated and presumed to result from mobilization of mature neutrophils. Our data provide a previously unidentified mechanism of how tumor-derived G-CSF induces a systemic expansion of neutrophils that are phenotypically different from mature neutrophils and the development of Rb1^{low} neutrophils in cancer. In addition, we showed that a single tumor-derived factor regulates both the development and activity of T cell-suppressive Ly6G$^+$ neutrophils in cancer.

Although we showed that G-CSF is the driving factor inducing the production and systemic expansion of T cell-suppressive neutrophils in the PyMT mouse model of cancer, other tumor-derived hematopoietic cytokines such as GM-CSF and IL-6 can

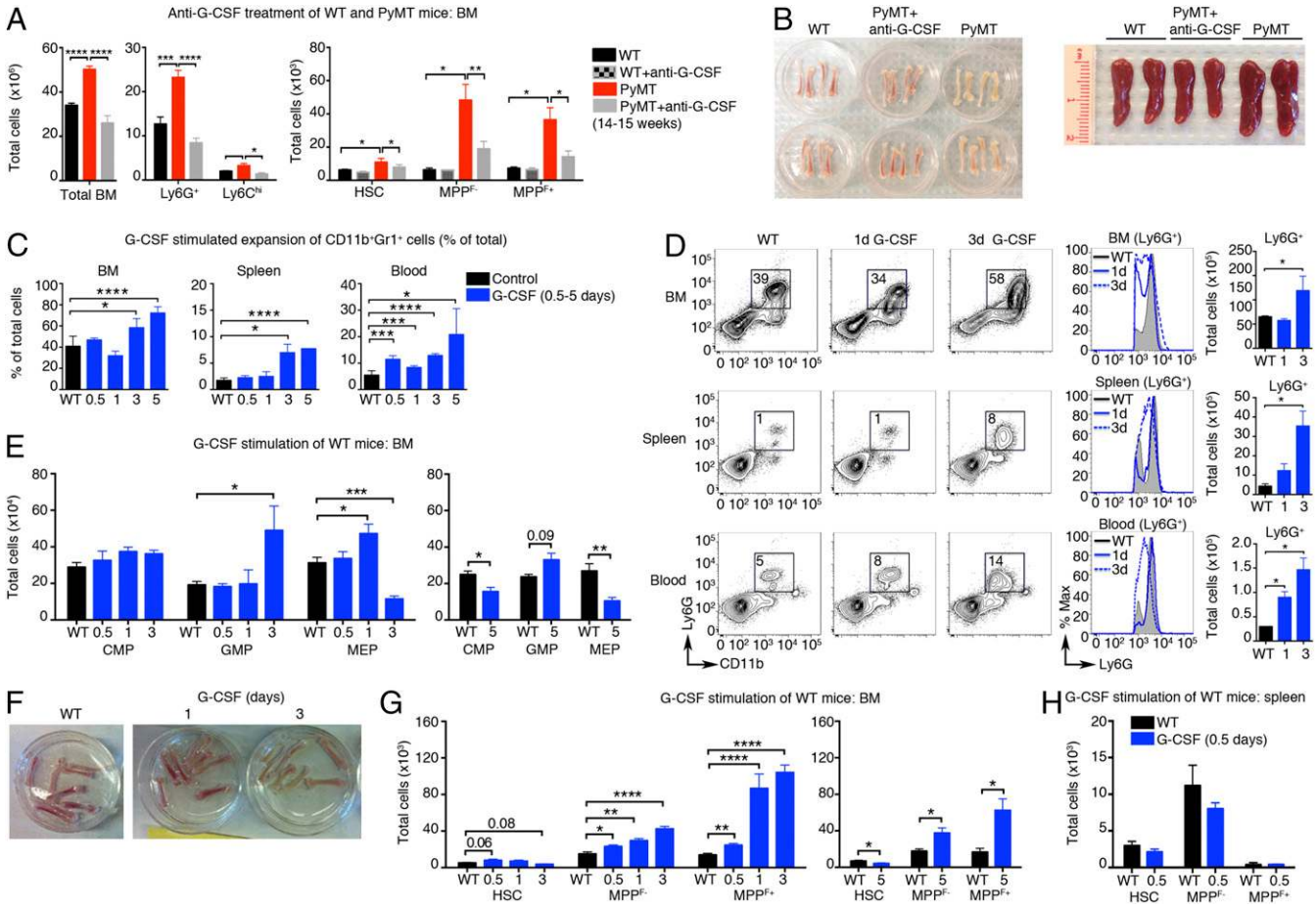

Fig. 5. Kinetics of G-CSF stimulation reveal G-CSF targets expansion of HSC and MPP populations in the BM. (*A* and *B*) BM, blood, spleen, lung, and MG (tumor) were harvested from WT FVB/n and PyMT mice (14–15 wk) or anti–G-CSF–treated mice. (*A*) Quantification of total BM cells (*Left*), cell numbers of Ly6G$^+$ and Ly6C^{hi} cells (*Center*), and cell numbers of HSC, MPP^{F+}, and MPP^{F-} populations (*Right*) in BM. (*B*) Representative images of femurs and tibias (*Left*) and spleens (*Right*). (*C–H*) BM, spleen, and blood were harvested from WT and G-CSF–stimulated (0.5–5 consecutive days) FVB/n mice. (*C*) Summary of the frequency (% total) of CD11b$^+$Gr1$^+$ cells assessed by flow cytometry. (*D*) FACS plots illustrate the frequency (% of total) of Ly6G$^+$ cells in BM, spleen, and blood (*Left*), histograms of Ly6G expression in Ly6G$^+$ cells (*Center*), and total cell numbers of Ly6G$^+$ cells (*Right*). (*E*) Cell numbers of CMPs, GMPs, and MEPs in BM. (*F*) Representative images of femurs and tibias. Cell numbers of (*G*) HSCs, MPPs^{F+}, and MPPs^{F-} in BM and (*H*) HSCs, MPPs^{F+}, and MPPs^{F-} in spleen. Data are representative of (*A* and *B*) three experiments (mean ± SEM, $n = 3$–7) and (*C–H*) two experiments (mean ± SEM, $n = 3$–10). *$P < 0.05$, **$P < 0.01$, ***$P < 0.005$, ****$P < 0.001$.

generate T cell-suppressive CD11b$^+$Gr1$^+$ myeloid cells (or MDSCs) (27). In addition, other myeloid populations, such as CSF-1–dependent tumor-associated macrophages (38, 39), can impair T-cell function and contribute to immune suppression. In an eloquent study by Elpek et al. (40), two different types of tumors with distinct myeloid cell compositions were implanted into the same mouse, and yet the immune compositions were unaffected by the presence of the other tumor type. This study shows that the tumor type dictates the immune composition of myeloid cells within the tumor and suggests different tumor types may elicit different cytokines.

In human cancer, multiple reports are now revealing that the T cell-suppressive myeloid cells that copurify in the mononuclear fraction, but are negative for macrophage and dendritic mature myeloid markers, are in fact activated, ROS-producing CD15$^+$ CD66b$^+$ neutrophils (41, 42). Of note, T-cell proliferation is highly suppressed by a subset of CD15$^+$/CD16^{low} neutrophils that expand in the blood of terminal cancer patients (43). Similar to Ly6G in mice, CD16 expression increases on human neutrophils with maturation (44) and is decreased on newly produced, but not mobilized, mature neutrophils in healthy volunteers after G-CSF stimulation (45). It is intriguing to speculate that G-CSF could be driving the production of CD16^{low} immunosuppressive neutrophils in cancer patients and that targeting G-CSF in these patients in combination with an immunotherapy that targets T-cell activation may increase antitumor efficacy and possibly even NK function (46). However, neutrophils in healthy individuals, with low levels of G-CSF, do not inhibit T-cell function and are essential for wound repair and protection from infection. Thus, future studies are warranted to assess the relationship between G-CSF concentration, neutrophil-mediated T-cell inhibition, and the protumor role of G-CSF.

Interestingly, ROS-producing neutrophils from tumor-bearing mice and human cancer patients can kill tumor cells directly ex vivo and when adoptively transferred into mice can inhibit lung metastasis (47). However, endogenous neutrophils in tumor-bearing mice do not appear to exhibit this antitumor phenotype and, in fact, exhibit a protumor phenotype (15). One possible explanation for these somewhat contradictory phenotypes is that the first study evaluated the potential of neutrophils to kill tumor cells when removed from the tumor microenvironment, whereas the latter study evaluated their ability. ROS production by neutrophils can be inhibited in hypoxic environments (48), and thus, it is possible that the hypoxic tumor microenvironment prevents neutrophils from killing tumor cells. Of note, we found late-stage tumor-bearing

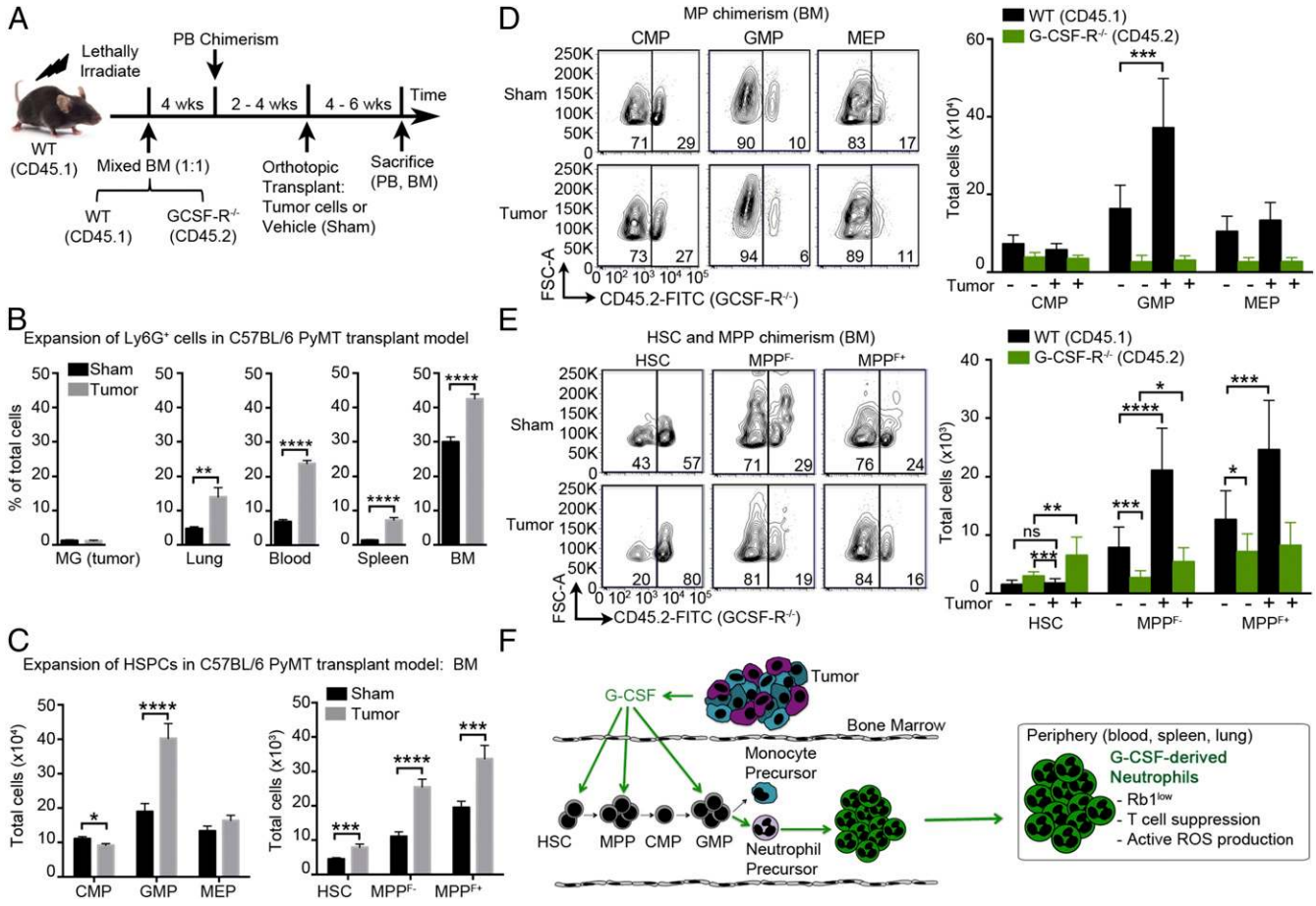

Fig. 6. Intrinsic G-CSF signaling is required in MPPs for altered myeloid differentiation in breast cancer. Mixed BM chimera (WT:G-CSF-R$^{-/-}$ at 1:1) C57BL/6 mice were transplanted with C57BL/6 PyMT primary tumor cells to evaluate chimerism. (*A*) Schematic illustrating experimental approach. (*B*) Summary of the frequency (% of total) of Ly6G$^+$ cells in lung, blood, spleen, and BM. (*C*) Cell numbers of CMP, GMP, MEP, HSC, MPP^{F-}, and MPP^{F+} populations in BM. (*D* and *E*) Representative FACS plots illustrate chimerism (*Left*) and quantification of cell numbers (*Right*) of CMP, GMP, MEP, HSC, MPP^{F-}, and MPP^{F+} populations in BM of tumor transplanted or sham-treated mixed BM chimera mice. (*F*) Model for the generation of activated, T cell-suppressive neutrophils in breast cancer. Tumor-derived G-CSF induces expansion of immature hematopoietic compartments, before the level of CMPs, resulting in reprogramming of the BM and expansion of activated, Rb1^{low} and T cell-suppressive neutrophils in peripheral tissues. Data are representative of (*A*–*E*) four experiments (mean ± SEM, $n = 8$). $^*P < 0.05$, $^{**}P < 0.01$, $^{***}P < 0.005$, $^{****}P < 0.001$.

mice to succumb to anemia due to a decrease in RBC production in BM, which paralleled the increasing myeloid production. Anemia could further contribute to a hypoxic environment and exacerbate the protumor role of neutrophils in cancer.

Skewing of HSPC differentiation toward the myeloid lineage has been reported in mouse models (30, 49) and in human patients (50) with different types of solid tumors, but until now the mechanism responsible was not known. Our data demonstrate a previously unidentified mechanism for the production of T cell-suppressive neutrophils in which early compartments of the hematopoietic hierarchy in BM are regulated by tumor-derived G-CSF. Expansion of these early BM compartments by G-CSF could provide a constant supply of lineage-committed progenitors during tumor-induced production of Ly6G$^+$ neutrophils. This would also explain the increased number of granulocyte-macrophage colony-forming units observed in BM of HER2 transgenic BALB/c tumor-bearing mice (49), and the increased numbers of circulating HSPCs observed in the blood of human patients with different types of carcinomas that also show elevated G-CSF levels (50). The pleiotropic mechanisms by which G-CSF regulates myeloid progenitor differentiation and proliferation (51), apoptosis of mature neutrophils (52), and priming of neutrophil activation (53), together with our previously unidentified observations of expansion of HSCs and MPPs, support the hypothesis that pathways involved in immune activation are also linked to early hematopoiesis to fulfill the demand of the immune system (35).

The role of neutrophils in human cancer has just begun to emerge, but a strong relationship between an increase in circulating neutrophils, referred to as a high neutrophil-to-lymphocyte ratio (NLR), and poor prognosis has been reported for decades; however, only recently were these reports compiled in a meta-analysis and shown to be an independent prognostic factor for poor survival in solid tumor cancers in more than 100 studies and 40,000 patients (54). In mice, tumor-associated neutrophils (TANs) and immunosuppressive neutrophils (PMN-MDSCs) promote tumor progression and metastasis by T cell-dependent and independent mechanisms, including promoting angiogenesis and remodeling of the extracellular matrix (55). Of interest, the tumor-promoting activity of TANs can be reversed to an anti-tumor role with anti-TGFβ blockade (56). Although these two populations of neutrophils are reported as distinct populations, it is becoming increasing clear that T cell-suppressive neutrophils are closely related to TANs (55). Thus, future studies are warranted to evaluate the effect of anti-TGFβ blockade on the T cell-suppressive role of neutrophils in cancer.

The essential role of BM-derived precursors of myeloid origin in promoting early tumor progression was first shown by Lyden et al. (57), who revealed that tumor-secreted VEGF recruits endothelial precursors that are essential for tumor angiogenesis. Little is known about the long-range systemic effects of tumor-derived factors on distant microenvironments (58), although there is evidence that tumor-derived factors can activate BM cells to provide a supportive systemic environment to promote growth of distant tumors (59–62). We demonstrated that tumor production of G-CSF induces chronic activation of myeloid differentiation in the BM, which ultimately results in inefficient erythropoiesis, anemia, and enlarged spleens to meet the demands of neutrophil and RBC cell production during tumor progression. Our data significantly increase our understanding of how tumors regulate the BM to generate T cell-suppressive neutrophils in cancer.

Materials and Methods

Mice. All mouse experiments were approved by the Institutional Animal Care and Use Committee of the University of California San Francisco, in accordance with the guidelines of the National Institutes of Health. Transgenic PyMT (MMTV-PyMT^{634Mul}/J) mice (21, 22) were maintained on FVB/n and C57BL/6 backgrounds; littermate controls were used for all experiments. WT FVB/n female mice were purchased from Charles River and WT C57BL/6 female (CD45.1 or CD45.2) mice were purchased from the Jackson (JAX) Laboratories for cross-breeding, in vivo G-CSF stimulation, or BM transplants. Homozygous C57BL/6 mice lacking expression of the receptor for G-CSF (G-CSF-R$^{-/-}$) (63) were provided by Daniel Link, Washington University, St. Louis, and then later acquired from JAX [B6.129 × 1(Cg)-Csf3r^{tm1Link}/J], with age-matched WT C57BL/6 (JAX) mice used as controls.

Flow Cytometry. All antibodies are listed in Table S2. Cells were blocked with rat IgG (10 μg/mL; Sigma) for at least 20 min on ice, washed with staining media [2% (vol/vol) HI, FBS in HBSS (BSS) without Ca^{2+} or Mg^{2+}, denoted SM], and then stained with fluorescently conjugated antibodies in SM for 30 min on ice, unless stated otherwise. For evaluation of MPs and HSPCs in BM and spleen, cells were stained as previously described (64). In brief, a six-step staining procedure was used that included the following combinations of antibodies: (*i*) mixture of unconjugated rat antibodies to lineage specific markers (B220, CD3, CD4, CD5, CD8, CD11b, Ter119, Gr1); (*ii*) fluorescently-tagged (PE-Cy5 or PE-Cy5.5) anti-rat secondary antibody; (*iii*) rat IgG (as described above) to block nonspecific binding; (*iv*) mixture of biotin- or fluorophore-conjugated antibodies to c-Kit, Sca-1, FcγR, and CD34 (for staining MPs) or c-Kit, Sca-1, Flk2, CD48, and CD150 (for staining HSPCs); (*v*) streptavidin conjugated to a fluorophore; and (*vi*) propidium iodide to identify live and dead cells. In some experiments evaluating mature myeloid cells (i.e., Gr1$^+$, Ly6G$^+$, or Ly6C^{hi}), stained cells were fixed with 2% (vol/vol) PFA at 4 °C overnight and analyzed 24–48 h later. For evaluation of intracellular Rb1 protein expression using flow cytometry, cell were stained for extracellular cell surface markers, fixed in 4% (vol/vol) PFA, permeabilized briefly (5 min) in 0.1% Triton X-100, blocked for 20 min at 4 °C with the 2.4G2 Fc-blocking antibody, and then stained with an anti-Rb1 antibody for 30 min on ice. The data were acquired with the FACSCalibur, LSRII, or FACSAria instruments (BD Biosciences) and analyzed using the FlowJo software (Tree Star, Inc.).

Isolation of Epithelial-Enriched Cells from Tumors. Tumors were digested in collagenase as described above, with several modifications. Tumors were digested for 30 min in collagenase media, centrifuged, DNase I treated, and then resuspended in DMEM complete. Single cells (which consisted primarily of stromal cells) were then removed from the cell suspension by a series of brief centrifugations (500 × *g* for 1 s, four times), which resulted in epithelial-enriched organoids (65). Organoids were then further digested in DMEM complete with trypsin (0.05% in EDTA) and DNase I (20 U/mL) for 20 min at 37 °C. Digestion was stopped by the addition of 10% (vol/vol) heat inactivated (HI) FBS in DMEM complete. Resulting epithelial-enriched cells were washed, filtered (as described above) and then cultured for in vitro assays or frozen in DMEM/F12 with 30% (vol/vol) HI FBS, 100 U/mL penicillin and 100 μg/mL streptomycin (P/S), and 10% (vol/vol) DMSO for in vivo transplant experiments.

Cell Lines. An MMTV-PyMT (FVB/n) cell line (66), which we refer to as VO-PyMT, was stably transduced with GFP and luciferase, as previously described (67).

Conditioned Media from Tumor Cells. Primary epithelial-enriched tumor cells (C57BL/6 PyMT) were cultured in 24-well plates at 4 × 10^5 cells/mL for 48 h in DMEM/F-12 medium with 1% FBS and P/S. VO-PyMT cells were cultured for 48 h in DMEM/F-12 medium and P/S (no FBS) with a final concentration of ∼1 × 10^6 cells/mL. Tumor cell-conditioned media were centrifuged at 800 × *g* for 5 min, and then supernatant was collected and stored at −80 °C.

In Vivo Studies and Reagents. Murine G-CSF (Peprotech) and a blocking antibody to murine G-CSF (R&D Diagnostics), along with the isotype control antibody, were prepared per manufacturer's instructions. For in vivo stimulation, 2 μg (in 200 μL) of G-CSF were injected s.c. daily, unless indicated otherwise. Fifty micrograms (in 100 μL) anti-G-CSF or isotype control antibody was injected i.p. every 48 h (total of four injections) for ∼1 wk, unless stated otherwise.

In Vivo BrdU Proliferation. Mice were injected i.p. with 100 μL (10 mg/mL) BrdU (BD Pharmingen) 2 or 24 h before death. Cells, isolated from multiple tissues, were first stained for extracellular surface markers, fixed, and permeabilized using the BD Cytofix/Cytoperm buffer (15 min at room temperature), washed, and then stored at 4 °C overnight. The next day, intracellular BrdU was stained according to the FITC BrdU Flow Kit Staining Protocol (BD Pharmingen). Following BrdU staining, cells were stored at 4 °C overnight, and data were then acquired on a BD LSR II flow cytometer and analyzed using FlowJo software.

BM Transplantation. Total BM cells from donor mice (CD45.1 WT and CD45.2 G-CSF-R$^{-/-}$ C57BL/6) (63) were collected from femurs by flushing. Cells were passed through a 70-μm filter, RBCs were lysed, and then cells were resuspended at 1:1 with a total of 3 × 10^6 cells/100 μL in SM. Congenic recipient mice (CD45.1 WT C57BL/6) were irradiated using a cesium source irradiator with a lethal dose (9 Gy) delivered in two doses (4.5 Gy) 3 h apart and were given antibiotic-containing water (1.l g/L neomycin sulfate and 10 U/L of polymyxin B sulfate) for 4 wk after irradiation as described previously (64).

Statistics. All of the data are expressed as mean ± SD or SEM as indicated. GraphPad Prism6 was used for all statistical analysis. *P* values were generated using the unpaired Student *t* test and considered significant when <0.05. In analysis of some experiments, normalization was performed by dividing individual raw data values (such as median fluorescent intensity values acquired by flow cytometry) by the mean of WT samples in that experiment.

ACKNOWLEDGMENTS. We thank D. Link (Washington University) for providing G-CSF-R–deficient mice, M. Lohela and V. Plaks for maintaining colonies of WT and MMTV-PyMT (FVB/n and C57BL/6) mice, Y. Yu and E. Atamaniuc for mice husbandry and genotyping, J. Chou for providing GFP/luciferase-expressing VO-PyMT cells, and N. Shah for the use of the ViCell XR cell viability instrument. Flow cytometry data were generated with the help of M. Kissner in the University of California, San Francisco, Parnassus Flow Cytometry Core, supported by NIH Diabetes Research Center Grant P30DK063720. This study was supported by grants from National Institutes of Health (NIH) Grants R01CA057621, R01CA180039, and P01AI053194 (to Z.W.) and R01HL092471 (to E.P.), a Leukemia and Lymphoma Society Scholar award (to E.P.), and a National Cancer Institute Traineeship Grant T32 CA108462 (to A-J.C.).

1. McAllister SS, Weinberg RA (2010) Tumor-host interactions: A far-reaching relationship. *J Clin Oncol* 28(26):4022–4028.
2. Quail DF, Joyce JA (2013) Microenvironmental regulation of tumor progression and metastasis. *Nat Med* 19(11):1423–1437.
3. Psaila B, Lyden D (2009) The metastatic niche: Adapting the foreign soil. *Nat Rev Cancer* 9(4):285–293.
4. Coussens LM, Werb Z (2002) Inflammation and cancer. *Nature* 420(6917):860–867.
5. de Visser KE, Eichten A, Coussens LM (2006) Paradoxical roles of the immune system during cancer development. *Nat Rev Cancer* 6(1):24–37.
6. Elinav E, et al. (2013) Inflammation-induced cancer: Crosstalk between tumours, immune cells and microorganisms. *Nat Rev Cancer* 13(11):759–771.
7. Grivennikov SI, Greten FR, Karin M (2010) Immunity, inflammation, and cancer. *Cell* 140(6):883–899.
8. Diaz-Montero CM, et al. (2009) Increased circulating myeloid-derived suppressor cells correlate with clinical cancer stage, metastatic tumor burden, and doxorubicin-cyclophosphamide chemotherapy. *Cancer Immunol Immunother* 58(1):49–59.
9. Gabrilovich DI, Ostrand-Rosenberg S, Bronte V (2012) Coordinated regulation of myeloid cells by tumours. *Nat Rev Immunol* 12(4):253–268.

10. Baniyash M, Sade-Feldman M, Kanterman J (2014) Chronic inflammation and cancer: Suppressing the suppressors. *Cancer Immunol Immunother* 63(1):11–20.
11. Kusmartsev S, et al. (2003) All-trans-retinoic acid eliminates immature myeloid cells from tumor-bearing mice and improves the effect of vaccination. *Cancer Res* 63(15): 4441–4449.
12. Sinha P, Clements VK, Bunt SK, Albelda SM, Ostrand-Rosenberg S (2007) Cross-talk between myeloid-derived suppressor cells and macrophages subverts tumor immunity toward a type 2 response. *J Immunol* 179(2):977–983.
13. Nozawa H, Chiu C, Hanahan D (2006) Infiltrating neutrophils mediate the initial angiogenic switch in a mouse model of multistage carcinogenesis. *Proc Natl Acad Sci USA* 103(33):12493–12498.
14. Yan HH, et al. (2010) Gr-1+CD11b+ myeloid cells tip the balance of immune protection to tumor promotion in the premetastatic lung. *Cancer Res* 70(15):6139–6149.
15. Kowanetz M, et al. (2010) Granulocyte-colony stimulating factor promotes lung metastasis through mobilization of Ly6G+Ly6C+ granulocytes. *Proc Natl Acad Sci USA* 107(50):21248–21255.
16. Ostrand-Rosenberg S, Sinha P (2009) Myeloid-derived suppressor cells: Linking inflammation and cancer. *J Immunol* 182(8):4499–4506.
17. Wilcox RA (2010) Cancer-associated myeloproliferation: Old association, new therapeutic target. *Mayo Clin Proc* 85(7):656–663.
18. Orkin SH, Zon LI (2008) Hematopoiesis: An evolving paradigm for stem cell biology. *Cell* 132(4):631–644.
19. Pietras EM, et al. (2014) Re-entry into quiescence protects hematopoietic stem cells from the killing effect of chronic exposure to type I interferons. *J Exp Med* 211(2): 245–262.
20. Youn JI, et al. (2013) Epigenetic silencing of retinoblastoma gene regulates pathologic differentiation of myeloid cells in cancer. *Nat Immunol* 14(3):211–220.
21. Guy CT, Cardiff RD, Muller WJ (1992) Induction of mammary tumors by expression of polyomavirus middle T oncogene: A transgenic mouse model for metastatic disease. *Mol Cell Biol* 12(3):954–961.
22. Lin EY, et al. (2003) Progression to malignancy in the polyoma middle T oncoprotein mouse breast cancer model provides a reliable model for human diseases. *Am J Pathol* 163(5):2113–2126.
23. Daley JM, Thomay AA, Connolly MD, Reichner JS, Albina JE (2008) Use of Ly6G-specific monoclonal antibody to deplete neutrophils in mice. *J Leukoc Biol* 83(1):64–70.
24. Fleming TJ, Fleming ML, Malek TR (1993) Selective expression of Ly-6G on myeloid lineage cells in mouse bone marrow. RB6-8C5 mAb to granulocyte-differentiation antigen (Gr-1) detects members of the Ly-6 family. *J Immunol* 151(5):2399–2408.
25. Movahedi K, et al. (2008) Identification of discrete tumor-induced myeloid-derived suppressor cell subpopulations with distinct T cell-suppressive activity. *Blood* 111(8): 4233–4244.
26. Youn JI, Nagaraj S, Collazo M, Gabrilovich DI (2008) Subsets of myeloid-derived suppressor cells in tumor-bearing mice. *J Immunol* 181(8):5791–5802.
27. Youn JI, Gabrilovich DI (2010) The biology of myeloid-derived suppressor cells: The blessing and the curse of morphological and functional heterogeneity. *Eur J Immunol* 40(11):2969–2975.
28. Hestdal K, et al. (1991) Characterization and regulation of RB6-8C5 antigen expression on murine bone marrow cells. *J Immunol* 147(1):22–28.
29. Liu T, et al. (2014) Gr-1+CD11b+ cells facilitate Lewis lung cancer recurrence by enhancing neovasculature after local irradiation. *Sci Rep* 4:4833.
30. Cortez-Retamozo V, et al. (2012) Origins of tumor-associated macrophages and neutrophils. *Proc Natl Acad Sci USA* 109(7):2491–2496.
31. Waight JD, Hu Q, Miller A, Liu S, Abrams SI (2011) Tumor-derived G-CSF facilitates neoplastic growth through a granulocytic myeloid-derived suppressor cell-dependent mechanism. *PLoS ONE* 6(11):e27690.
32. Maruyama K, et al. (2012) The transcription factor Jdp2 controls bone homeostasis and antibacterial immunity by regulating osteoclast and neutrophil differentiation. *Immunity* 37(6):1024–1036.
33. Dumortier A, Kirstetter P, Kastner P, Chan S (2003) Ikaros regulates neutrophil differentiation. *Blood* 101(6):2219–2226.
34. Richards MK, Liu F, Iwasaki H, Akashi K, Link DC (2003) Pivotal role of granulocyte colony-stimulating factor in the development of progenitors in the common myeloid pathway. *Blood* 102(10):3562–3568.
35. Manz MG, Boettcher S (2014) Emergency granulopoiesis. *Nat Rev Immunol* 14(5): 302–314.
36. Schuettpelz LG, et al. (2014) G-CSF regulates hematopoietic stem cell activity, in part, through activation of Toll-like receptor signaling. *Leukemia* 28(9):1851–1860.
37. Lord BI, et al. (1989) The kinetics of human granulopoiesis following treatment with granulocyte colony-stimulating factor in vivo. *Proc Natl Acad Sci USA* 86(23): 9499–9503.
38. Zhu Y, et al. (2014) CSF1/CSF1R blockade reprograms tumor-infiltrating macrophages and improves response to T-cell checkpoint immunotherapy in pancreatic cancer models. *Cancer Res* 74(18):5057–5069.
39. Strachan DC, et al. (2013) CSF1R inhibition delays cervical and mammary tumor growth in murine models by attenuating the turnover of tumor-associated macrophages and enhancing infiltration by CD8(+) T cells. *OncoImmunology* 2(12):e26968.
40. Elpek KG, et al. (2014) The tumor microenvironment shapes lineage, transcriptional, and functional diversity of infiltrating myeloid cells. *Cancer Immunol Res* 2(7): 655–667.
41. Schmielau J, Finn OJ (2001) Activated granulocytes and granulocyte-derived hydrogen peroxide are the underlying mechanism of suppression of t-cell function in advanced cancer patients. *Cancer Res* 61(12):4756–4760.
42. Brandau S, Moses K, Lang S (2013) The kinship of neutrophils and granulocytic myeloid-derived suppressor cells in cancer: Cousins, siblings or twins? *Semin Cancer Biol* 23(3):171–182.
43. Choi J, et al. (2012) CD15+/CD16low human granulocytes from terminal cancer patients: Granulocytic myeloid-derived suppressor cells that have suppressive function. *Tumour Biol* 33(1):121–129.
44. Elghetany MT (2002) Surface antigen changes during normal neutrophilic development: A critical review. *Blood Cells Mol Dis* 28(2):260–274.
45. Kerst JM, et al. (1993) Recombinant granulocyte colony-stimulating factor administration to healthy volunteers: Induction of immunophenotypically and functionally altered neutrophils via an effect on myeloid progenitor cells. *Blood* 82(11):3265–3272.
46. Sceneay J, et al. (2012) Primary tumor hypoxia recruits CD11b+/Ly6Cmed/Ly6G+ immune suppressor cells and compromises NK cell cytotoxicity in the premetastatic niche. *Cancer Res* 72(16):3906–3911.
47. Granot Z, et al. (2011) Tumor entrained neutrophils inhibit seeding in the premetastatic lung. *Cancer Cell* 20(3):300–314.
48. McGovern NN, et al. (2011) Hypoxia selectively inhibits respiratory burst activity and killing of Staphylococcus aureus in human neutrophils. *J Immunol* 186(1):453–463.
49. Melani C, Chiodoni C, Forni G, Colombo MP (2003) Myeloid cell expansion elicited by the progression of spontaneous mammary carcinomas in c-erbB-2 transgenic BALB/c mice suppresses immune reactivity. *Blood* 102(6):2138–2145.
50. Wu WC, et al. (2014) Circulating hematopoietic stem and progenitor cells are myeloid-biased in cancer patients. *Proc Natl Acad Sci USA* 111(11):4221–4226.
51. Zhang H, et al. (2010) STAT3 controls myeloid progenitor growth during emergency granulopoiesis. *Blood* 116(14):2462–2471.
52. van Raam BJ, Drewniak A, Groenewold V, van den Berg TK, Kuijpers TW (2008) Granulocyte colony-stimulating factor delays neutrophil apoptosis by inhibition of calpains upstream of caspase-3. *Blood* 112(5):2046–2054.
53. Balazovich KJ, Almeida HI, Boxer LA (1991) Recombinant human G-CSF and GM-CSF prime human neutrophils for superoxide production through different signal transduction mechanisms. *J Lab Clin Med* 118(6):576–584.
54. Templeton AJ, et al. (2014) Prognostic role of neutrophil-to-lymphocyte ratio in solid tumors: A systematic review and meta-analysis. *J Natl Cancer Inst* 106(6):dju124.
55. Dumitru CA, Lang S, Brandau S (2013) Modulation of neutrophil granulocytes in the tumor microenvironment: Mechanisms and consequences for tumor progression. *Semin Cancer Biol* 23(3):141–148.
56. Fridlender ZG, et al. (2009) Polarization of tumor-associated neutrophil phenotype by TGF-beta: "N1" versus "N2" TAN. *Cancer Cell* 16(3):183–194.
57. Lyden D, et al. (2001) Impaired recruitment of bone-marrow-derived endothelial and hematopoietic precursor cells blocks tumor angiogenesis and growth. *Nat Med* 7(11): 1194–1201.
58. Peinado H, Lavotshkin S, Lyden D (2011) The secreted factors responsible for premetastatic niche formation: Old sayings and new thoughts. *Semin Cancer Biol* 21(2): 139–146.
59. McAllister SS, et al. (2008) Systemic endocrine instigation of indolent tumor growth requires osteopontin. *Cell* 133(6):994–1005.
60. Peinado H, et al. (2012) Melanoma exosomes educate bone marrow progenitor cells toward a pro-metastatic phenotype through MET. *Nat Med* 18(6):883–891.
61. Hattori K, et al. (2002) Placental growth factor reconstitutes hematopoiesis by recruiting VEGFR1(+) stem cells from bone-marrow microenvironment. *Nat Med* 8(8): 841–849.
62. Kaplan RN, et al. (2005) VEGFR1-positive haematopoietic bone marrow progenitors initiate the pre-metastatic niche. *Nature* 438(7069):820–827.
63. Liu F, Wu HY, Wesselschmidt R, Kornaga T, Link DC (1996) Impaired production and increased apoptosis of neutrophils in granulocyte colony-stimulating factor receptor-deficient mice. *Immunity* 5(5):491–501.
64. Santaguida M, et al. (2009) JunB protects against myeloid malignancies by limiting hematopoietic stem cell proliferation and differentiation without affecting self-renewal. *Cancer Cell* 15(4):341–352.
65. Welm BE, Dijkgraaf GJ, Bledau AS, Welm AL, Werb Z (2008) Lentiviral transduction of mammary stem cells for analysis of gene function during development and cancer. *Cell Stem Cell* 2(1):90–102.
66. Halpern J, et al. (2006) The application of a murine bone bioreactor as a model of tumor: Bone interaction. *Clin Exp Metastasis* 23(7-8):345–356.
67. Chou J, et al. (2013) GATA3 suppresses metastasis and modulates the tumour microenvironment by regulating microRNA-29b expression. *Nat Cell Biol* 15(2):201–213.

Supporting Information

Casbon et al. 10.1073/pnas.1424927112

SI Materials and Methods

Histology. MGs, tumors, or lungs were fixed in 4% PFA at 4 °C overnight and then processed for paraffin. Five-micrometer paraffin sections were cut, transferred to slides, and stained for H&E.

Tissue Collection and Cell Isolation. For all primary cell suspensions, red blood cells (RBCs) were removed by lysis in ammonium-chloride-potassium (ACK) buffer at room temperature for 5 min and washed with SM, and then total remaining live cells were counted using a Vi-Cell XR Cell Viability Analyzer (Beckman Coulter).

Peripheral blood. Peripheral blood (PB) was collected in the chest cavity after cutting the right atrium and injecting 15 mL of 0.01 M EDTA in Dulbecco's PBS (D-PBS) through the left ventricle using a 20-G needle to flush the vasculature and collect total PB cells. PB was then mixed 1:1 with 2% Dextran for 0.5–2 h, supernatants were collected and centrifuged, and any remaining RBCs were lysed. In some experiments, PB was collected directly from the chest cavity (after cutting the right atrium) using a 1-mL syringe. This PB was allowed to clot at room temperature and centrifuged at 500 × *g* at 4 °C for 10 min, and then the supernatant (serum) was stored at −80 °C in aliquots.

Lung. Following PB collection, the lungs were removed, and individual lobes were isolated. The left lobe was fixed in 4% PFA for histology, whereas the other lobes were minced, resuspended in DMEM/F-12 (Gibco) complete medium (5 μg/mL insulin and 50 μg/mL gentamicin; Sigma-Aldrich) with collagenase type IV (2 mg/mL; Sigma-Aldrich), and digested at 37 °C on a shaker for 45–60 min. Digested tissues were then centrifuged, DNase I (20 U/mL; Sigma-Aldrich) treated for 2–3 min, washed, and passed through a 70-μm filter followed by a 40-μm filter, and finally the RBCs were lysed.

Mammary glands and tumors. Four MGs (MG 3′s and 4's) were harvested from all WT or PyMT mice with early disease (6–10 wk), one MG 4 was fixed in 4% PFA, and the other three MGs were minced and collagenase digested as described above for lungs. The LN from MG 4 was always removed before mincing. For PyMT mice with more progressive disease (12–15 wk), only the largest tumor was collected, half the tumor was fixed, and the other half was collagenase digested.

Spleen. Spleens were passed through a 40-μm filter, washed, and filtered again, and finally RBCs were lysed.

Bone marrow. Femurs, tibias, and the long bones of the arms were harvested, cleaned, crushed using a mortar and pestle, and passed through a 70-μm filter, RBCs were lysed, and BM cells were enriched using Histopague 1119 (Sigma-Aldrich). In some experiments, femurs were flushed to collect total BM cells, where indicated.

Transplant of C57BL/6 MMTV-PyMT Primary Tumors. Epithelial-enriched tumor cells were isolated from transgenic C57BL/6 MMTV-PyMT tumors and frozen as described above. The day of transplants, cells were thawed, washed in DMEM/F12 medium that contained 10% FBS and P/S, washed twice, resuspended in PBS, and then mixed 1:1 with Matrigel Complete (BD Biosciences). A total of 4×10^6 cells in 40 μL were injected into fat pads of each MG 4 (8×10^6 cells per mouse). Cohorts of mice were killed when the first tumor reached end stage (20 mm in length).

Quantitative Real-Time PCR to Assess Lung Metastasis. In some experiments, single cell suspensions of lung cells were pelleted and stored at −80 °C. Total RNA was isolated from lung cell pellets using the RNeasy Mini Kit (Qiagen). cDNA was synthesized from 0.1 to 1 mg of total RNA using the iScript Reverse Transcription Supermix kit (Bio-Rad) according to the manufacturer's protocols. Real-time PCR amplification was performed using FastStart Universal SYBR Green master mix (Roche Applied Science) in an Eppendorf Mastercycler realplex^2 machine (Eppendorf). PCR amplification conditions were as follows: initial DNA denaturation for 10 min at 95 °C, followed by two steps of 95 °C for 15 s and 60 °C for 1 min, for a total 40 cycles. Samples were run in duplicate for at least three independently obtained biological samples for each experimental condition. Ct values were normalized to β-actin, and relative expression was calculated using the $2^{-\Delta\Delta Ct}$ method. For mouse β-actin, the forward primer sequence was 5′-CACAGCTTCTTTGC and the reverse primer sequence was 5′-CGTCATCCATGGCG. For PyMT, the forward primer sequence was 5′-CCAACAGATACACCCGCACAT and the reverse primer sequence was 5′-GGGCTCAGCAACACAAGGAT.

Superoxide Production. PB and lung cells were isolated as described above with a few modifications. Lung cells were not digested in collagenase, but instead were minced in 0.1% BSA in HBSS without Ca^{2+} or Mg^2+ (buffer 3) and then passed through a 40-μm filter to limit activation of neutrophils during the isolation process. PB and lung cells were washed and stained with a fluorescently tagged antibody to Ly6G in 0.1% BSA in HBSS without Ca^{2+} or Mg^{2+} instead of SM and a blocking antibody was not used. Dihydrorhodamine (DHR) was used to measure superoxide production in Ly6G$^+$ cells (1, 2). After staining the cells for Ly6G, cells were resuspended at 1–2 × 10^6 cells/mL in PBS-EGG (1 mM EDTA, 0.05% gelatin, and 0.09% D-glucose) and labeled with 0.1 μM DHR 123 (Molecular Probes) for 30 min at 37 °C. The reaction was stopped by placing the cells on ice, adding cold PBS-EGG, and then centrifuging for 5 min at 500 × *g*. The superoxide production of Ly6G$^+$ neutrophils was analyzed by flow cytometry using a FACSCalibur within 30 min of stopping the reaction. For evaluation of superoxide in Ly6G$^+$ cells from G-CSF–stimulated mice, 5 μg/mouse was injected for 5 consecutive days.

Cell Morphology. Cells isolated from multiple tissues were stained with fluorescently conjugated antibodies to CD45, CD11b, Ly6G, and Ly6C as described above. CD45$^+$CD11b$^+$Ly6G$^+$Ly6C^{int} cells were double sorted by flow cytometry into 30% serum, which yielded a greater than 95% purity. Cells were then centrifuged at 200 × *g*, resuspended in DMEM/F12 with 30% FBS and P/S at 2.5–7.5 × 10^4 cells/150 μL, transferred to glass slides using a Cytofuge2 (StatSpin, set at 8.5 for 5 min), dried overnight, and then stained with Wright-Giemsa.

T-Cell Proliferation. CD11b$^+$Ly6G$^+$ cells were double sorted by flow cytometry from WT and PyMT (FVB/n) (14–15 wk of age) splenocytes. Total splenocytes from WT mice served as the T-cell source to evaluate proliferation. A total of 5 × 10^6 total splenocytes in 1 mL buffer 2 (5% FBS in HBSS without Ca^{2+} or Mg^{2+}) were labeled with 5 μM carboxyfluorescein diacetate succinimidyl ester (CFSE; eBioscience) for 5 min at room temperature. Then, 10 mL of buffer 2 was added, and cells were placed on ice for 5–10 min. Cells were washed twice with buffer 2 and then once with RPMI complete medium (5% FBS, 10 mM Hepes, 2 mM L-glutamine, P/S, and 5.5 μM β-mercaptoethanol). Finally, CFSE-labeled splenocytes (1 × 10^5 cells per well of 96-well plate) were stimulated with plate-bound activating antibodies to CD3 (0.5 μg/mL) and CD28 (1 μg/mL) in the presence

or absence of $CD11b^+Ly6G^+$ cells (1×10^5 cells per well). After 4 d of culture, plates were centrifuged, supernatants were collected and cultured to confirm there was no contamination, and cells were stained with fluorescently conjugated antibodies to TCRβ, CD4, and CD8, along with a live/dead marker (either DAPI or Sytox Blue) to evaluate T-cell proliferation in live cells.

Western Blotting. Protein expression of Rb1 was evaluated by Western blotting in total cells or FACS-sorted $CD11b^+Ly6G^+$ cells from the spleens of WT and PyMT mice (14–15 wk) or WT mice treated with control (PBS) or G-CSF (2 μg/mouse per day). For total cells from the spleen, equal protein (10–60 μg) was loaded per well. For $Ly6G^+$ sorted cells, $0.3–1 \times 10^6$ cells were loaded per well. Protein was resolved by SDS/PAGE under reducing conditions and transferred to PVDF membranes (Bio-Rad). The membrane was first incubated with a primary antibody to mouse Rb1 and then followed by an HRP-conjugated secondary antibody along with a primary antibody to mouse β-actin that was directly conjugated to HRP. Immunoreactive bands were visualized by enhanced chemiluminescence using Supersignal West Femto Maximum Sensitivity Substrate (Pierce) on a LAS-4000 (Fuji-Film Life Sciences).

Whole Blood Analysis of RBCs and Hemoglobin. Blood was drawn from mice by tail bleed and placed in BD Microtainer blood collection tubes containing EDTA (BD Biosciences). Blood analysis was performed using the HEMAVET 950 hematology analyzer (Drew Scientific) in accordance with the manufacturer's recommendation.

Multiplex Analysis of Cytokines and Chemokines. The concentration of a panel of 32 cytokines and chemokines was measured in serum from WT and PyMT mice and tumor cell-conditioned media using multiplex LASER bead technology (Eve Technologies). All samples were run in duplicate. To control for any species cross-reaction with cytokines or chemokines in bovine serum, DMEM/F-12 medium with 1% FBS and P/S alone was run in duplicate and subtracted as background from conditioned medium samples. We also measured the concentration of G-CSF by ELISA (Quantikine kit; R&D) in some serum samples to confirm the accuracy of the multiplex technology and found that results were similar.

1. Vowells SJ, Sekhsaria S, Malech HL, Shalit M, Fleisher TA (1995) Flow cytometric analysis of the granulocyte respiratory burst: A comparison study of fluorescent probes. *J Immunol Methods* 178(1):89–97.

2. Smith JA, Weidemann MJ (1993) Further characterization of the neutrophil oxidative burst by flow cytometry. *J Immunol Methods* 162(2):261–268.

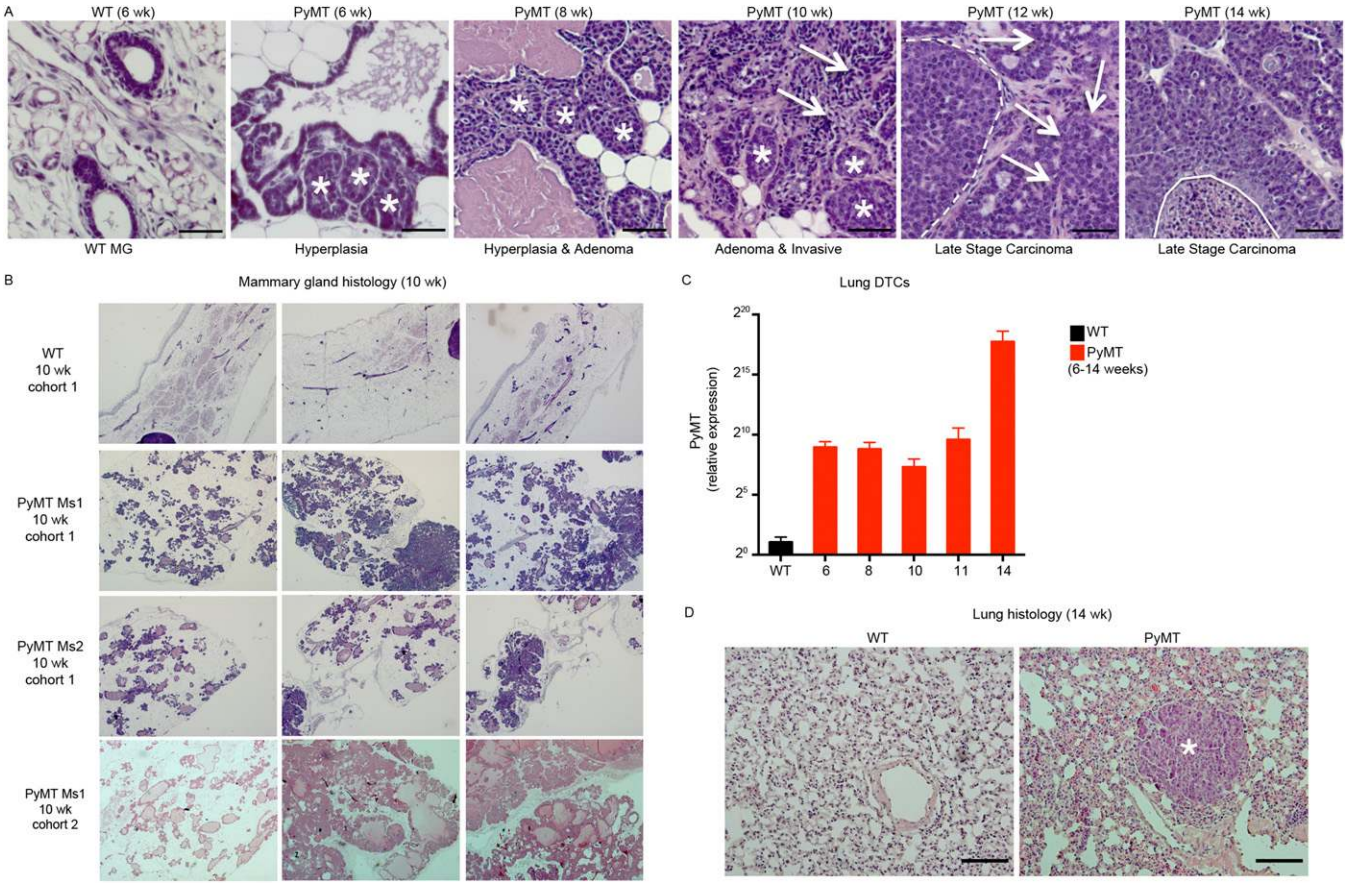

Fig. S1. Characterization of tumor progression and lung metastasis in FVB/n PyMT mice. (*A* and *B*) H&E-stained mammary glands (MGs) or tumors from WT and PyMT mice. (*A*) At 6 wk, MGs of PyMT mice show atypical ductal hyperplasia with epithelial cells arranged in small, well-defined nodules around ducts (asterisks). By 8 wk, nodules increased in number and in size as cells began to fill duct lobular units, indicating adenoma or mammary intraepithelial neoplasia (MIN). By 10 wk, MGs in PyMT mice had areas of hyperplasia and adenoma/MIN and the beginning of invasion into the surrounding stroma (arrows). By 12 wk, most tumors were invasive carcinoma with large disorganized nodules still present in some areas (dotted line). By 14 wk, necrotic areas (solid line) were prominent within tumors. (Scale bar, 50 μm.) (*B*) Multiple MG sections from WT littermate and PyMT mice at 10 wk illustrate that a large proportion of PyMT MGs still have areas that lack tumor development and appear WT-looking. (*C*) Relative cDNA expression of the PyMT transgene was evaluated by qPCR in cells isolated from lungs of WT and PyMT mice. Error bars denote SEM. (*D*) H&E-stained lung sections from a WT and PyMT mouse (14 wk). Asterisk denotes a lung metastasis. (Scale bar, 100 μm.) Data are representative of (*A* and *B*) four experiments at 6 wk ($n = 6$) or six experiments at each time point from 8 to 15 wk ($n = 8–12$), (*C*) two experiments at each time point 6–14 wk ($n = 3–6$), and (*D*) six experiments ($n = 12$).

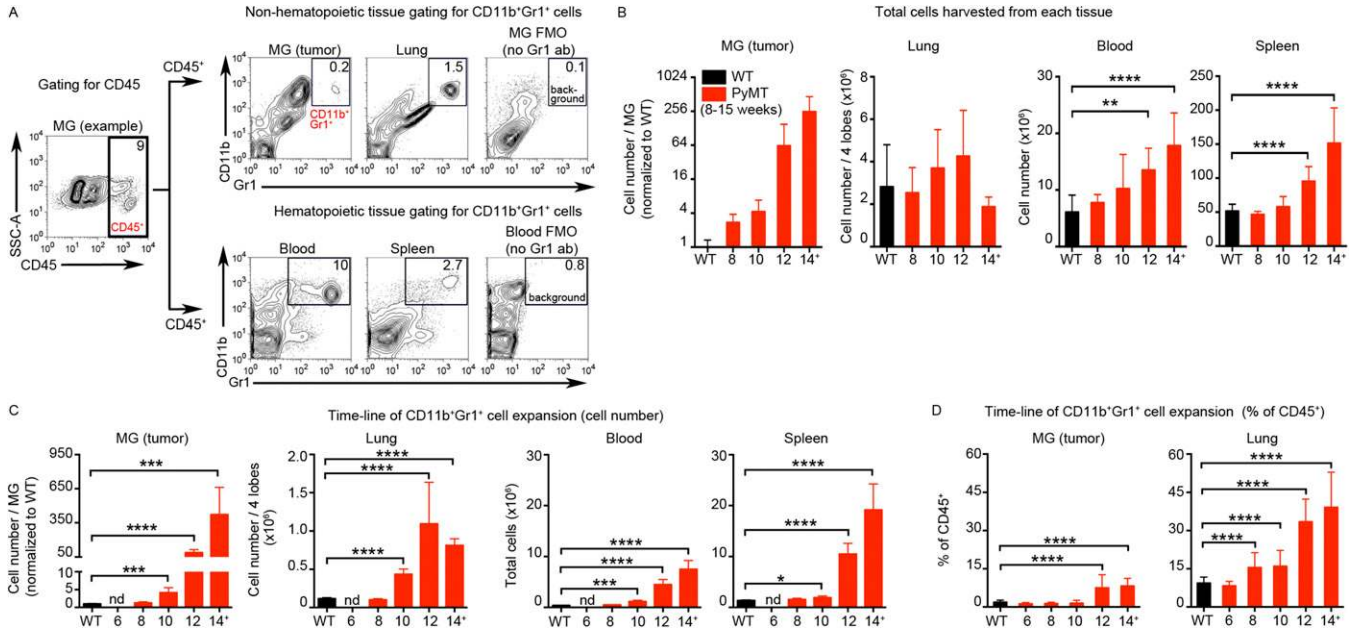

Fig. S2. Expansion of CD11b$^+$Gr1$^+$ cells during tumor progression in FVB/n PyMT mice. (*A*) Representative FACS plots show the gating strategy to evaluate the frequency of CD11b$^+$Gr1$^+$ cells in nonhematopoietic tissues (MGs, tumors, or lungs) and hematopoietic tissues (blood and spleen). The frequency of CD45$^+$ cells in a MG (*Left*) and CD11b$^+$Gr1$^+$ cells in the indicated tissues (*Right*) from a WT mouse (14 wk) are shown as examples. Values within gates are % of total cells. Gates for CD11b and Gr1 double-positive cells were selected based on a fluorescence minus one (FMO) control in which cells were stained with all antibodies except the Gr1 antibody (no Gr1 antibody). (*B*) Summary of the number of cells isolated from MGs (tumors), lungs, blood, and spleens in WT and PyMT mice during tumor progression (8–14 wk). Graph depicts mean ± SD. (*C*) Quantification of the number of CD11b$^+$Gr1$^+$ cells in WT and PyMT mice (6–15 wk). Graph depicts mean ± SEM. Cell numbers from mice of 6 wk were not determined (nd). (*D*) Quantification of the frequency of CD11b$^+$Gr1$^+$ cells within the immune infiltration (% of CD45$^+$) in MG (tumor) and lung of WT and PyMT mice. Graph depicts mean ± SD. Data are representative of (*A*–*D*) six experiments at each time point from 8 to 15 wk (n = 8–12) or four experiments from 6 wk (n = 6).

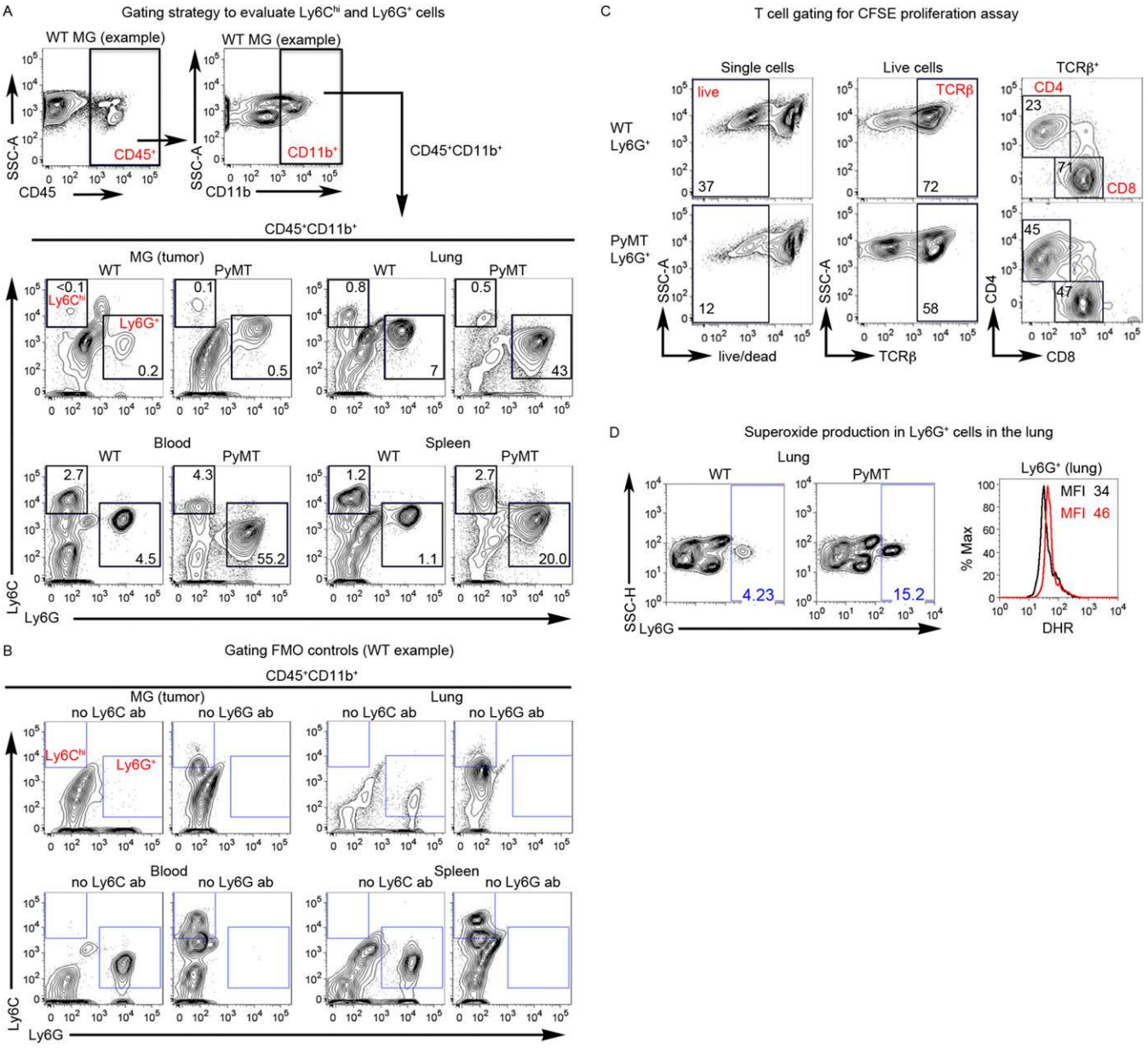

Fig. S3. Characterization of Ly6G$^+$ cells in late-stage FVB/n PyMT mice. (*A*) Gating strategy and representative FACS plots of Ly6G$^+$ and Ly6C^{hi} cells in MG (tumor), lung, blood, and spleen from WT and PyMT mice (14–15 wk). Values displayed within gates are the frequency (% of total) of Ly6G$^+$ or Ly6C^{hi} cells in the indicated tissues. (*B*) Gates for Ly6G$^+$ and Ly6C^{hi} cells were selected based on standard FMO controls in which either the anti-Ly6C or anti-Ly6G antibody (ab) was not included in the ab mix (denoted as no Ly6C or no Ly6G). (*C*) Gating strategy and representative FACS plots of CD4$^+$ and CD8$^+$ T cells after 4 d of CD3/CD28 stimulation in the presence of Ly6G$^+$ cells from spleens of WT or PyMT FVB/n mice (14–15 wk). Values shown are the frequency of cells within each parent gate. (*D*) Representative FACS plots illustrate the gating and frequency (% of total) of Ly6G$^+$ cells in lungs (*Left*) and histogram show DHR fluorescence in Ly6G$^+$ cells (*Right*) from WT (black line) and PyMT (red line) mice (14–15 wk). Data are representative from (*A* and *B*) six experiments (n = 12–15), (*C*) two experiments (n = 4), and (*D*) three experiments (n = 5–6).

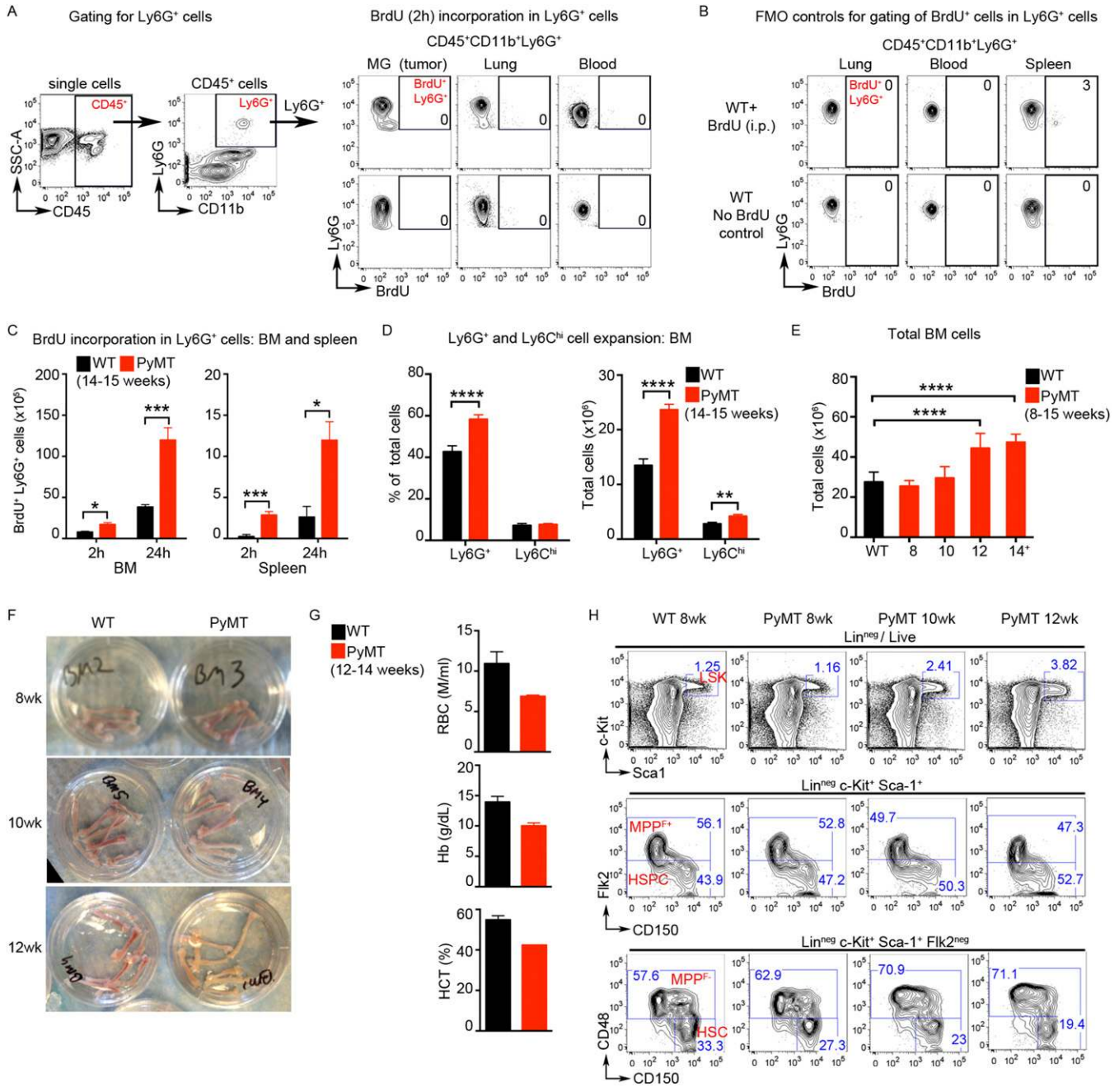

Fig. S4. Characterization of myeloid cell development in BM of FVB/n PyMT mice. (*A*) Representative FACS plots illustrate the gating to assess BrdU incorporation in Ly6G$^+$ cells in MG (tumor), lung, and blood from WT and PyMT mice (14–15 wk) after a 2-h BrdU pulse. (*B*) Representative FACS plots illustrate the lack of BrdU$^+$ Ly6G$^+$ cells in a control WT mouse not injected with BrdU. (*A* and *B*) Values displayed within gates are the frequency of Ly6G$^+$ cells that are BrdU$^+$. (*C*) Total cell number of BrdU$^+$ Ly6G$^+$ cells in BM and spleen after 2- and 24-h BrdU pulses. (*D*) Frequency (% of total) and cell number of Ly6G$^+$ and Ly6C^{hi} cells in BM (14–15 wk). (*E*) Total cells in BM of WT and PyMT mice (8–14 wk). (*F*) Representative images of femurs and tibias harvested from WT and PyMT mice (8–12 wk). (*G*) RBC, hemoglobin (Hb), and hematocrit (HCT) values in blood from WT and PyMT mice (12–14 wk). (*H*) Representative FACS plots illustrate gating and frequency of HSPCs in BM of WT and PyMT mice (8–12 wk). Values shown are the frequency of cells within each parent gate. Data are representative of (*A* and *B*) three experiments, (*C*) two experiments (mean ± SEM, n = 3–5 mice per group), (*D*) six experiments (mean ± SEM, n = 9–11), (*E*) three or four experiments (mean ± SD, n = 6–9), (*F* and *H*) two or three experiments at each time point (n = 3–4), and (*G*) two experiments (mean ± SEM, n = 2–4).

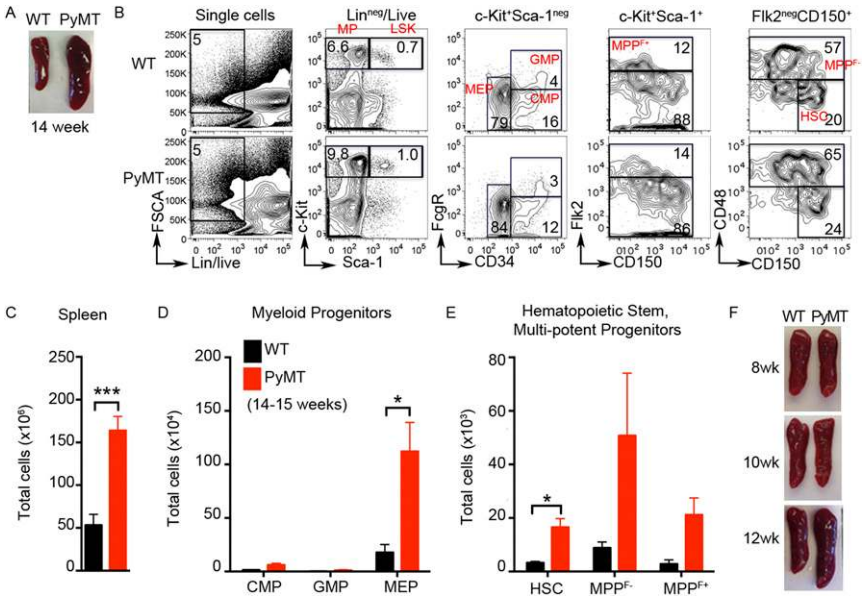

Fig. S5. In contrast to BM, expansion of myeloid progenitors in the spleen of late-stage FVB/n PyMT mice is predominantly due to expansion of MEPs. (*A*–*E*) Spleens from WT and PyMT mice (14–15 wk) were evaluated by flow cytometry for changes in HSPCs and myeloid progenitors. (*A*) Representative image of spleens from WT and PyMT mice. (*B*) Gating and representative FACS plots for HSC and MP populations in spleens. Values shown are the frequency within each parent gate. (*C*) Total cell number in spleens from WT and PyMT mice. Total cell number of (*D*) CMP, MEP, and GMP and (*E*) HSC, MPP^{F-}, and MPP^{F+} populations in spleens from WT and PyMT mice. (*F*) Representative images of spleens from WT and PyMT mice (8–12 wk) during tumor progression. Representative data from (*A*–*E*) three experiments (mean ± SEM, $n = 3$–4) and (*F*) two experiments ($n = 3$–4).

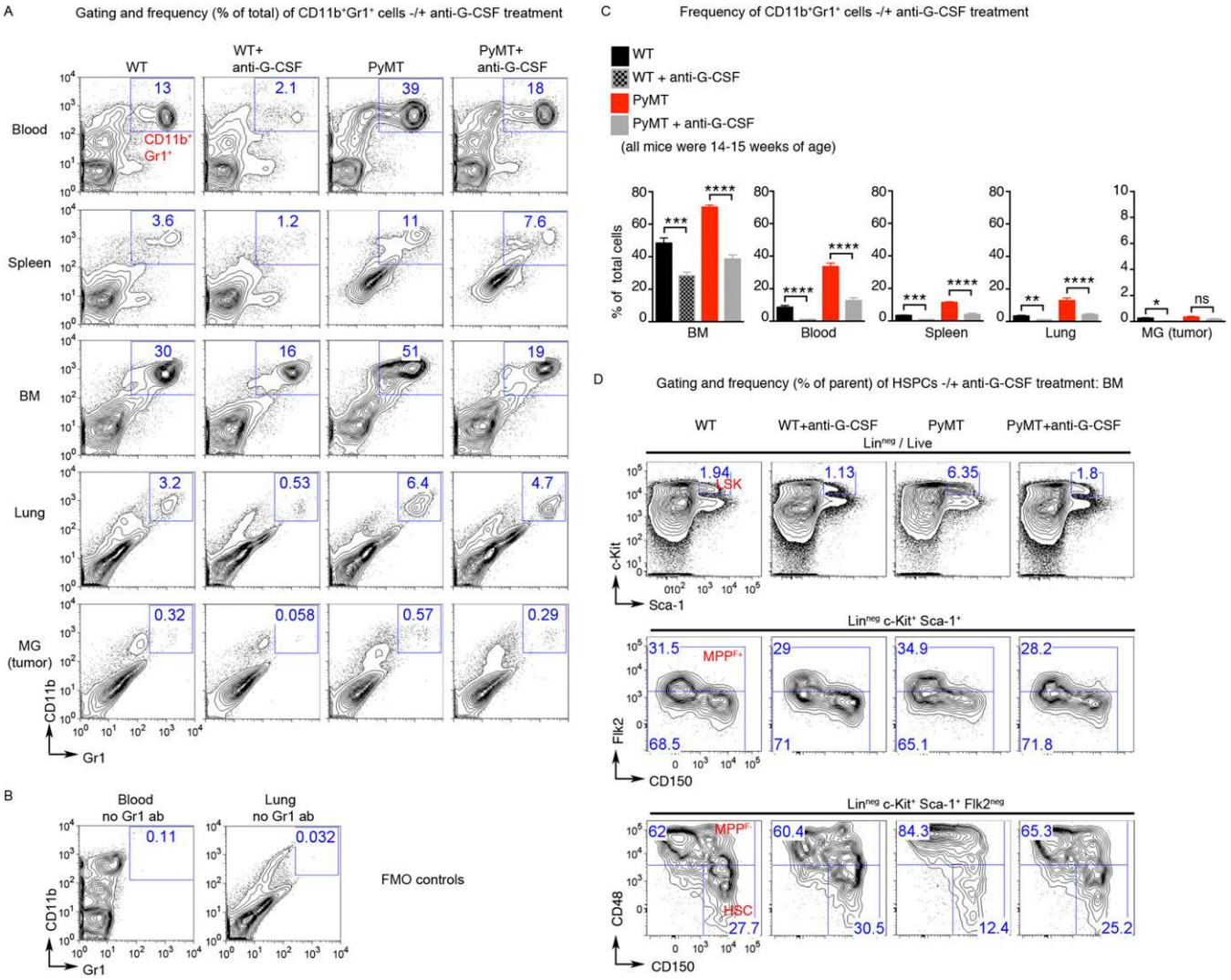

Fig. S6. Anti–G-CSF treatment reduces CD11b^{+}Gr1^{+} cells and HSPCs in BM of FVB/n PyMT mice. (*A*) Representative FACS plots illustrate gating and frequency (% of total) of CD11b^{+}Gr1^{+} cells in the blood, spleen, BM, lung, and MG (tumor) from WT and PyMT mice (14–15 wk). (*B*) Representative FACS plots illustrate CD11b staining in the absence of Gr1 staining (FMO control), which was used to select Gr1-positive gates for hematopoietic tissues (based on gating with blood cells) and for nonhematopoietic tissues (based on gating with lung cells). (*C*) Summary of CD11b^{+}Gr1^{+} cells in WT and PyMT mice ± anti–G-CSF treatment. Graph depicts mean ± SEM. (*D*) Representative FACS plots of LSK, MPP^{F+}, MPP^{F-}, and HSC populations in the BM of WT and PyMT mice ± anti–G-CSF treatment. Values shown are the frequency of cells within each parent gate. Data are representative from (*A*–*D*) three independent experiments (n = 3–7).

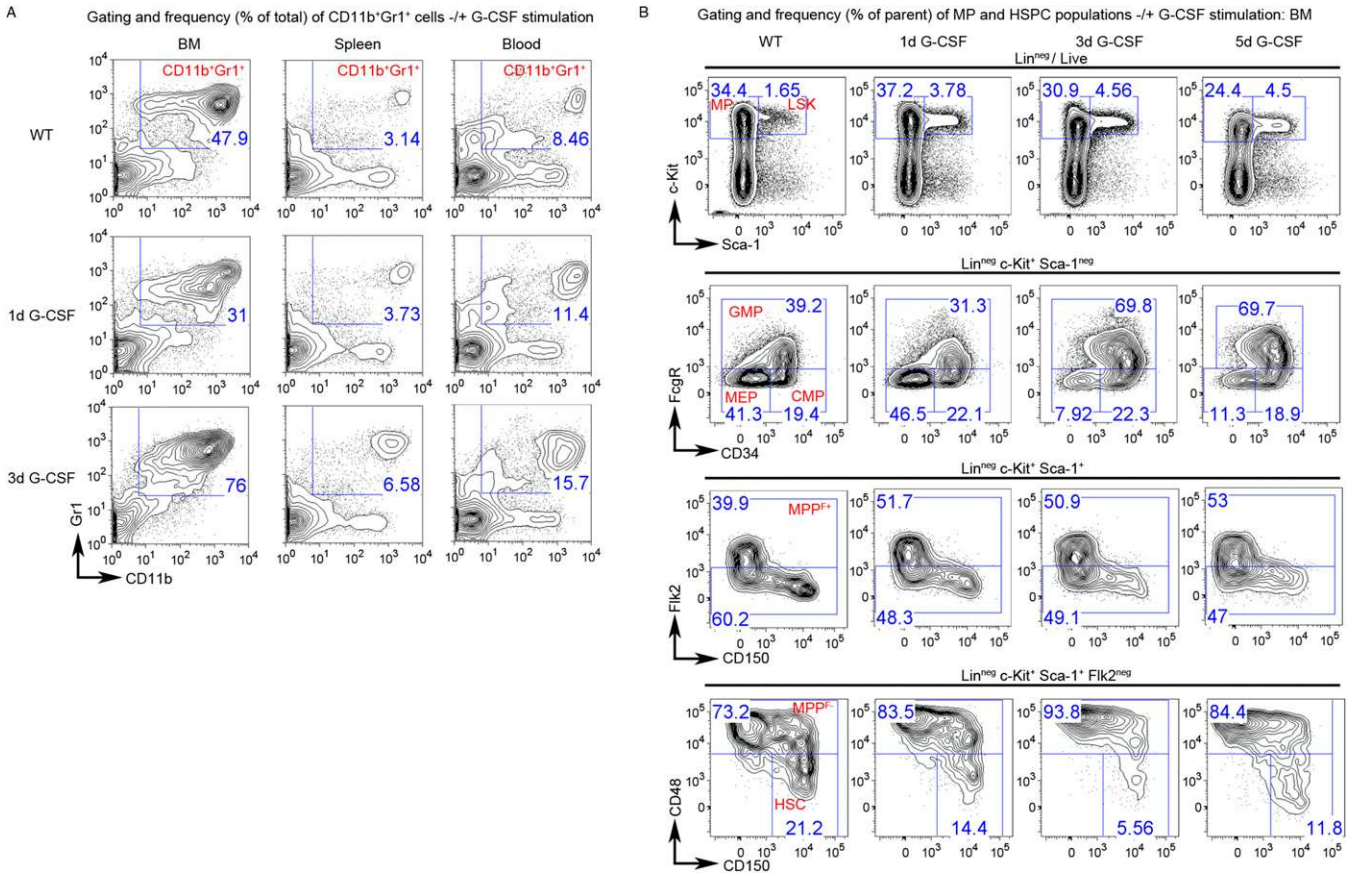

Fig. S7. G-CSF stimulation increases CD11b^{+}Gr1^{+} cells and HSPCs in BM of FVB/n PyMT mice. Representative FACS plots illustrate (*A*) gating and frequency (% of total) of CD11b^{+}Gr1^{+} cells in the BM, spleen, and blood and (*B*) gating and frequency (% of parent) of LSK, MPP^{F+}, MPP^{F-}, and HSC populations in the BM of WT ± G-CSF stimulation (1–5 d). Representative FACS plots from two independent experiments (n = 3–10).

Table S1. Protein concentration (pg/mL) of 32 chemokines and cytokines evaluated in the serum by multiplex analysis

	Mean			Mean			Mean			Mean			Mean		
Factor	WT ($n = 6$)	PyMT ($n = 6$)	6 wk (P)	WT ($n = 4$)	PyMT ($n = 7$)	8 wk (P)	WT ($n = 5$)	PyMT ($n = 7$)	10 wk (P)	WT ($n = 2$)	PyMT ($n = 4$)	12 wk (P)	WT ($n = 6$)	PyMT ($n = 6$)	14 wk (P)
M-CSF	10 ± 2	10 ± 1	0.872	3 ± 1	5 ± 1	0.578	6 ± 2	7 ± 2	0.644	4 ± 2	5 ± 2	0.891	8 ± 1	13 ± 1	0.029
G-CSF	275 ± 47	263 ± 42	0.856	131 ± 27	339 ± 80	0.092	195 ± 39	706 ± 137	0.012	116 ± 31	4558 ± 1335	0.091	371 ± 85	9534 ± 1405	0.000
GM-CSF	14 ± 6	18 ± 7	0.651	14 ± 6	4 ± 4	0.133	10 ± 3	16 ± 4	0.260	14 ± 14	5 ± 5	0.449	10 ± 4	20 ± 5	0.120
IFNy	1 ± 1	2 ± 1	0.476	3 ± 2	1 ± 1	0.270	2 ± 1	2 ± 1	0.469	3 ± 3	<1 ± <1	0.178	2 ± 1	1 ± <1	0.571
TNFa	3 ± 1	4 ± 1	0.437	1 ± <1	2 ± 1	0.167	3 ± 1	4 ± <1	0.184	2 ± <1	3 ± <1	0.119	3 ± <1	5 ± <1	0.001
VEGF	1 ± <1	1 ± <1	0.494	3 ± 1	3 ± 1	0.963	1 ± <1	1 ± <1	0.612	2 ± 1	4 ± 3	0.715	1 ± <1	9 ± 7	0.259
LIF	<1 ± <1	<1 ± <1	0.779	1 ± 1	1 ± <1	0.943	<1 ± <1	<1 ± <1	0.476	1 ± 1	2 ± 1	0.651	1 ± 1	1 ± <1	0.570
CCL2/MCP-1	35 ± 15	42 ± 10	0.691	26 ± 12	28 ± 8	0.939	49 ± 11	58 ± 7	0.505	10 ± 7	65 ± 13	0.047	39 ± 10	81 ± 5	0.003
CCL3/MIP-1a	20 ± 5	24 ± 4	0.462	9 ± 3	19 ± 3	0.075	19 ± 5	25 ± 5	0.452	15 ± 15	18 ± 2	0.763	21 ± 3	35 ± 3	0.009
CCL4/MIP-1b	35 ± 7	53 ± 11	0.193	17 ± 4	25 ± 5	0.365	46 ± 13	43 ± 9	0.850	14 ± 4	37 ± 5	0.036	38 ± 6	56 ± 4	0.024
CCL5/ RANTES	21 ± 4	24 ± 2	0.636	15 ± 2	15 ± 2	0.831	20 ± 6	22 ± 5	0.796	14 ± 6	21 ± 4	0.371	20 ± 3	25 ± 2	0.125
CCL11/ Eotaxin	722 ± 62	745 ± 32	0.752	614 ± 58	731 ± 65	0.264	905 ± 91	957 ± 84	0.691	746 ± 54	756 ± 47	0.900	713 ± 29	776 ± 65	0.399
KC/CXCL1	46 ± 15	39 ± 10	0.715	43 ± 5	47 ± 4	0.562	54 ± 17	85 ± 13	0.176	65 ± 1	86 ± 8	0.159	71 ± 6	89 ± 19	0.389
CXCL2/MIP-2	34 ± 8	46 ± 7	0.266	108 ± 55	98 ± 38	0.877	73 ± 7	77 ± 8	0.691	95 ± 65	53 ± 24	0.487	46 ± 11	43 ± 8	0.824
CXCL6/LIX	4,064 ± 1,006	3,855 ± 1,025	0.887	16,736 ± 9,140	10,412 ± 5,806	0.553	10,293 ± 1,929	8,381 ± 1,529	0.450	16,348 ± 14,373	9,634 ± 8,177	0.680	3,761 ± 1,376	2,315 ± 744	0.377
CXCL9/MIG	32 ± 3	31 ± 5	0.862	46 ± 9	44 ± 9	0.896	55 ± 11	53 ± 5	0.815	52 ± 16	40 ± 5	0.362	51 ± 7	43 ± 3	0.337
CXCL10/IP-10	56 ± 4	57 ± 5	0.832	50 ± 4	49 ± 3	0.819	52 ± 4	61 ± 2	0.043	49 ± 6	56 ± 2	0.281	50 ± 3	67 ± 3	0.002
IL-1a	191 ± 28	207 ± 26	0.684	342 ± 140	335 ± 107	0.972	218 ± 59	200 ± 40	0.795	334 ± 166	189	0.387	164	294	0.259
IL-1b	7 ± 2	8 ± 2	0.833	7 ± 2	5 ± 1	0.474	10 ± 1	11 ± 1	0.372	3 ± <1	4	0.533	9	9	0.758
IL-2	5 ± 2	4 ± 2	0.852	3 ± 1	2 ± 1	0.427	3 ± 1	5 ± 1	0.350	3 ± 1	1 ± <1	0.099	3	4	0.353
IL-3	1 ± <1	1 ± <1	0.934	1 ± <1	1 ± <1	0.920	1 ± <1	1 ± <1	0.642	<1 ± <1	1 ± <1	0.628	1	1	0.399
IL-4	<1 ± <1	<1 ± <1	0.295	<1 ± <1	<1 ± <1	0.945	<1 ± <1	<1 ± <1	0.162	<1 ± <1	<1 ± <1	0.055	0	0	0.795
IL-5	11 ± 3	11 ± 2	0.973	8 ± 1	10 ± 3	0.565	14 ± 4	17 ± 3	0.529	9 ± 1	8	0.786	9	10	0.233
IL-6	3 ± 1	2 ± <1	0.380	2 ± 1	1 ± <1	0.166	2 ± 1	5 ± 1	0.065	3 ± <1	15	0.525	4	8	0.027
IL-7	4 ± 2	6 ± 1	0.475	1 ± 1	1 ± <1	0.232	5 ± 1	18 ± 13	0.426	2 ± <1	1 ± <1	0.288	9	4	0.349
IL-9	26 ± 7	34 ± 12	0.577	2 ± 2	8 ± 4	0.242	22 ± 3	25 ± 5	0.654	15 ± 15	4	0.339	16	32	0.249
IL-10	3 ± 1	3 ± 1	0.975	2 ± 1	2 ± 1	0.970	4 ± <1	5 ± <1	0.060	3 ± 1	2	0.315	2	3	0.518
IL-12(p40)	39 ± 11	43 ± 8	0.748	19 ± 11	10 ± 6	0.465	31 ± 13	38 ± 9	0.665	25 ± 22	25	0.976	37	43	0.680
IL-12(p70)	28 ± 11	44 ± 11	0.306	18 ± 11	13 ± 5	0.625	20 ± 10	40 ± 9	0.180	26 ± 26	3	0.228	36	39	0.758
IL-13	23 ± 10	34 ± 7	0.380	3 ± 2	4 ± 1	0.513	27 ± 10	24 ± 6	0.786	1 ± 1	4	0.240	14	35	0.017
IL-15	7 ± 2	24 ± 9	0.089	19 ± 11	15 ± 7	0.757	12 ± 2	24 ± 9	0.276	17 ± 15	7	0.382	29	12	0.401
IL-17	1 ± <1	2 ± <1	0.299	1 ± <1	1 ± <1	0.652	1 ± <1	2 ± <1	0.416	1 ± 1	1 ± 1	0.844	2	2	0.553

Table S2. List of antibodies used in this study

Antibodies for flow cytometry	Clone or (catalog no.)	Distributor	Dilution or final concentration
Unconjugated lineage antibodies			
Anti-mouse B220	RA3-6B2	Biolegend	1:800
Anti-mouse CD3	17A2	Biolegend	1:200
Anti-mouse CD4	GK1.5	eBioscience	1:1,600
Anti-mouse CD5	53.7.3	eBioscience	1:800
Anti-mouse CD11b	M1/70	eBioscience	1:1,600
Anti-mouse Ter119	Ter119	eBioscience	1:400
Anti-mouse Gr1	RB6-8C5	eBioscience	1:800
Unconjugated additional antibodies			
Anti-CD3e activating antibody	145–2C11	UCSF Ab Core	0.5 μg/mL
Anti-CD28 activating antibody	37.51	UCSF Ab Core	1 μg/mL
Anti-CD16/CD32 Fc blocking antibody	2.4G2	Tonbo	10 μg/mL
Fluorescently conjugated			
Anti-BrdU	(559619)	BD Pharmingen	1:50
Anti-mouse B220	RA3-6B2	Biolegend	1:400
Anti-mouse c-Kit (Flt3)	2B8	Biolegend	1:800
Anti-mouse CD3	17A2	eBioscience	1:100
Anti-mouse CD4	GK1.5	eBioscience	1:100
Anti-mouse CD4	RM4-5	Tonbo	1:100
Anti-mouse CD8a	53–6.7	eBioscience	1:100
Anti-mouse CD11b (Mac1)	M1/70	eBioscience	1:400
Anti-mouse CD34	RAM34	eBioscience	1:25
Anti-mouse CD45	30-F11	eBioscience	1:200
Anti-mouse CD45.1	A20	Tonbo	1:100
Anti-mouse CD45.2	104	eBioscience	1:200
Anti-mouse CD48	HM48-1	Biolegend	1:400
Anti-mouse CD150	TC15-12F12.2	Biolegend	1:400
Anti-mouse EpCAM	G8.8	eBioscience	1:400
Anti-mouse FcγR (CD16/CD32)	93	eBioscience	1:50
Anti-mouse Flk2	A2F10	eBioscience	1:100
Anti-mouse Gr1	RB6-3C5	eBioscience	1:1,200
Anti-mouse Ly6C	HK1.4	eBioscience	1:600
Anti-mouse Ly6G	IA8	Biolegend	1:200
Anti-mouse/human Rb1	G3-245	BD Pharmingen	1:50
Anti-mouse Sca1	D7	Biolegend	1:200
Anti-mouse Tcrβ	H57-597	eBioscience	1:100
Isotype control for Rb1	MOPC-21	BD Pharmingen	1:50
In vivo blocking antibodies			
Anti-mouse G-CSF	67604 (mab414)	R&D	50 μg/mouse
Rat IgG control	43414 (mab005)	R&D	50 μg/mouse
Western blot antibodies			
Anti-mouse actin-HRP	C-11 (sc.1615)	Santa Cruz	1:10,000
Anti-Retinoblastoma 1	D20 (9313)	Cell Signaling	1:1,000
Anti-rabbit–HRP (second)	(ab7090)	Abcam	1:2,000